

VEGETATION PATTERN FORMATION VIA ENERGY-BALANCE-CONSTRAINED MODELING*

CHAD M. TOPAZ†

Abstract. Vegetation in semi-arid environments self-organizes into striking spatial patterns—bands, spots, labyrinths, and gaps—with characteristic wavelengths on the order of tens to hundreds of meters. Existing reaction-diffusion models postulate nonlinearities and transport laws from qualitative physical reasoning, making it hard to distinguish essential structural features from artifacts of the chosen forms. Here we show how energy-balance and water-conservation principles can constrain the admissible model class before a specific closure is chosen. These constraints motivate a family of semilinear closures; an Euler–Lagrange representative yields a fourth-order vegetation equation coupled to quasi-steady water transport on a one-dimensional hillslope. Linear stability analysis identifies three instability mechanisms: classical water-mediated feedback, energy-balance spatial coupling, and water deflection by vegetation gradients. Their balance depends on terrain geometry. On slopes, the water-mediated coupling dominates and the model reproduces two empirical observations: pattern wavelength increases with aridity, and vegetation bands migrate uphill. On flat terrain, the energy-balance spatial coupling can drive instability independently. Numerical simulations confirm the linear predictions, and exploratory continuation reveals a narrow hysteresis region consistent with subcritical bifurcation.

Key words. vegetation patterns, dryland ecology, energy balance, reaction-diffusion

MSC codes. 92D40, 35K57, 35B36, 35Q92

1. Introduction. Vegetation self-organizes into regular spatial patterns across semi-arid regions worldwide, including the Horn of Africa, the Australian outback, the American Southwest, and the Sahel. These patterns—bands, often called “tiger bush,” as well as spots, labyrinths, and gaps—have characteristic wavelengths on the order of tens to hundreds of meters [7, 23]. They occur on gentle slopes with gradients of 0.2–2% in regions receiving roughly 50–750 mm of annual rainfall [23].

These patterns share common features across continents, plant communities, and soil types [2]. As aridity increases along a rainfall gradient, gaps give way to labyrinths on flat terrain or bands on slopes, then to spots, and finally to bare soil [7]. The precise sequence depends on terrain geometry. The pattern wavelength increases with aridity, with drier sites producing more widely spaced bands or spots [8]. Vegetation bands on slopes tend to migrate uphill, with speeds on the order of a meter per year or less, though some sites show no detectable migration [8, 23].

The dominant theoretical framework uses reaction-diffusion equations. The foundational model of Klausmeier [16] couples vegetation density $n(\mathbf{x}, t)$ and soil water $w(\mathbf{x}, t)$ through

$$(1.1) \quad \frac{\partial w}{\partial t} = a - w - wn^2 + v \frac{\partial w}{\partial x}, \quad \frac{\partial n}{\partial t} = wn^2 - mn + D_n \nabla^2 n,$$

where a is rainfall, m is plant mortality, v is downhill water advection speed, and D_n is a plant diffusion coefficient. Subsequent models introduced soil water diffusion and density-dependent infiltration [24], surface and subsurface water compartments [19], and biomass-dependent infiltration, root augmentation, and soil-crust effects [11, 12]. See [9, 17, 18] for reviews. On the analysis side, detailed studies have deepened the

*Submitted to the editors April 6, 2026.

Funding: This work received no external funding.

†Department of Mathematics and Statistics, Williams College, Williamstown, MA, and Department of Applied Mathematics, University of Colorado Boulder, Boulder, CO (cmt6@williams.edu).

mathematical understanding. These include wavelength and migration speed analysis [21], existence and stability of periodic patterns via geometric singular perturbation theory [20], bifurcation-theoretic robustness of the pattern sequence [13], and a flow-kick framework for rainfall variability [10]. These models successfully reproduce the qualitative phenomenology—including the pattern sequence with increasing aridity, uphill band migration, and wavelength scaling—and have generated mathematical insight into pattern selection, multistability, and desertification transitions.

Despite this success, the models’ nonlinearities, spatial couplings, and functional forms are postulated from qualitative physical reasoning rather than derived from first principles, and different authors make different choices. Gilad and colleagues use nonlocal integral kernels whose widths depend on biomass for water uptake [12], while Klausmeier uses wn^2 [16]. Von Hardenberg and colleagues include soil water diffusion, while the original Klausmeier model does not [24]. Because models with different postulated forms all produce patterns, it is difficult to assess which structural choices are essential and which are artifacts.

The most systematic attempt to organize this modeling landscape is arguably the three-feedback framework of Gilad et al. [11, 12]. In the *infiltration feedback*, biocrusts on bare soil reduce infiltration, so water preferentially enters vegetated patches. In the *water uptake feedback*, roots extract water from a spatially extended zone, depleting surroundings; root augmentation enters as a spatial component of this mechanism. In the *shading feedback*, vegetation reduces evaporation from the soil surface beneath it. This three-feedback framework is a valuable organizing principle. However, all three feedbacks are water-mediated, describing different spatial pathways of vegetation–water interaction. It takes the functional forms as given and does not establish whether non-water-mediated instability pathways contribute.

Stepping back, we ask what structural constraints on a vegetation–water model can be derived from physical principles. By narrowing the admissible class before choosing a specific closure, we can separate physically enforced structure from closure-dependent artifacts. The answer involves three layers of constraint, which we develop in succession with progressively stronger assumptions.

First, energy-balance reasoning constrains the signs of local terms. The energy budgets of soil and vegetation are governed by micrometeorology [4, 14], but to our knowledge this has not been used as a starting point for vegetation pattern models. When the energy mismatch is expressed as a function of vegetation density and soil water, the leading coefficients have signs constrained by the dominant physics of semi-arid environments. Water loss is similarly constrained by mass conservation and the sign of evaporation and transpiration.

Second, smoothness and finite interaction range justify gradient expansion for all spatial terms. The energy fluxes at each point depend smoothly on the vegetation field in a spatial neighborhood, and the water flux depends on the local values of both vegetation and water and their spatial derivatives. Because the relevant interaction ranges are short relative to pattern wavelengths, gradient expansion constrains the derivative structure of all spatial coupling terms. On a hillslope, the downhill direction breaks left–right symmetry, so the expansion includes both symmetric and asymmetric interaction terms. An effective-density ansatz further reduces the coefficient functions to a small number of interaction parameters. Applied to the water flux, the gradient expansion recovers classical advection and diffusion and yields a deflection term proportional to the vegetation gradient.

Third, a variational closure provides a concrete evolution law. We close the vegetation dynamics with a semilinear variational ansatz based on a functional that

rewards biomass accumulation and penalizes departures from energy balance, with water determined as a quasi-steady functional of the vegetation field. This closure is an additional modeling assumption, analogous to choosing a specific PDE right-hand side in the Klausmeier framework. The resulting restricted class of semilinear closures shares a common quasi-steady water response and a dispersion relation that decomposes into local and water-coupling contributions. The Euler–Lagrange closure is distinguished within this class by additional algebraic structure: it forces the local contribution to be even in wavenumber and the quartic coefficient to be nonpositive. The resulting fourth-order spatial derivatives guarantee short-wavelength regularization. These play the same structural role as diffusion in the Klausmeier model, but at higher order and arising from the variational closure acting on the gradient-expanded energy mismatch rather than from a postulated dispersal mechanism.

The linearized dispersion relation decomposes exactly into a local even polynomial and a water-coupling contribution, identifying three instability mechanisms: classical water-mediated feedback, energy-balance spatial coupling, and water deflection by vegetation gradients. The role of energy-balance spatial coupling depends on hillslope geometry. On flat terrain, where the asymmetric interaction vanishes, it can drive finite-wavenumber instability alone. On slopes, the asymmetric interaction reduces this contribution, and the water-mediated coupling becomes the primary determinant of wavelength selection, producing longer wavelengths at lower rainfall in the studied parameter regimes. Numerical simulations confirm the wavelength predictions and reproduce uphill band migration in the nonlinear regime.

Section 2 develops the constrained model ingredients; section 3 defines the semilinear closure family and adopts the Euler–Lagrange representative on a one-dimensional hillslope; section 4 derives the dispersion relation and identifies three instability mechanisms; section 5 compares with existing models; section 6 tests the predictions numerically; and sections 7 and 8 discuss implications and open directions. The concrete model analyzed throughout is a one-dimensional specialization that uses only the plant energy subsystem and freezes certain coefficients at the steady state; the broader framework admits richer closures that we do not pursue.

2. Model formulation. We consider a one-dimensional transect of a semi-arid hillslope, with x pointing downhill. Two state variables describe the system: the vegetation density $u(x, t)$, measured as biomass per unit ground area, and the soil water content $w(x, t)$, measured as volume per unit ground area. The energy-balance constraints and gradient expansions developed in this section extend to two spatial dimensions; we restrict to a one-dimensional transect for the analysis and simulations that follow. This section develops the sign constraints and gradient-expansion structure from physical principles, without yet specifying a dynamical law for the vegetation. The result is a constrained class of admissible model ingredients: sign-constrained local energy mismatches, gradient-expansion forms for all spatial terms, and a quasi-steady water functional. Any concrete PDE closure, including the variational one in section 3, must draw from this class.

The development involves three kinds of modeling choices, which we distinguish throughout. *Physical/regime assumptions* are sign and shape constraints motivated by semi-arid energy balance and overland-flow hydraulics. *Mathematical approximations* include smoothness, Taylor truncation, and gradient expansion. *Modeling closures* are structural simplifications adopted for tractability rather than derived from first principles. Table 1 summarizes all assumptions and their roles; Table 2 collects all dimensional quantities.

TABLE 1

Summary of modeling assumptions. Each is classified as regime (sign/shape constraint from semi-arid physics), approx. (mathematical approximation), or closure (structural simplification for tractability).

Assumption	Type	Justification	Consequence
<i>Local energy mismatches</i> (section 2.1)			
Soil surplus at $(0, 0)$; signs of $\partial_u G_1^{(0)}$, $\partial_w G_1^{(0)}$	regime	semi-arid energy balance: radiation interception, moisture dissipation	coefficient signs in (2.1)
Plant deficit at low u ; single maximum; transpirational cooling	regime	bounded input, diminishing returns, transpiration	leading-order polynomial (2.2)
Smoothness & Taylor truncation of $G_i^{(0)}$	approx.	regularity of averaged energy budgets	polynomial forms (2.1)–(2.2)
<i>Spatial structure</i> (section 2.2)			
Gradient expansion of nonlocal interactions	approx.	short interaction range vs. pattern scale	spatial terms with u_x , u_{xx}
Effective-density ansatz	closure	single amplitude function, fixed profile shape	one free function η_i per subsystem
<i>Water conservation</i> (section 2.3)			
Signs of $\partial_w L$, $\partial_u L$	regime	moisture monotonicity; transpiration dominates shading	signs of μ_0 , μ_1 in (2.9)
Flux sign constraints	regime	gravity, diffusion, surface roughness	signs in (2.11)–(2.13)
Timescale separation	approx.	hours–days vs. seasons–decades	quasi-steady $W[u]$
<i>Variational closure</i> (section 3)			
Linear dependence on G , G_x , G_{xx}	closure	lowest-order tractable family	semilinear closure family (3.1)
EL representative of semilinear family	closure	even local symbol; nonpositive quartic	fourth-order vegetation PDE
Frozen $\eta = \eta(U_0, W_0)$	closure	slowly varying interaction amplitude; small G_0 regime	D shifted by $O(\mu)$; parity and $E \leq 0$ preserved
$s = 0$ (plant energy only)	closure	simplest single-subsystem representative; richer nonlinear structure in G_2	G_1 drops from vegetation dynamics

2.1. Local energy mismatch. The plant–soil system comprises two thermally distinct subsystems—soil and plants—each with its own energy budget. In reality, they depend on temperature, radiation, humidity, wind speed, and other variables. We define the local energy mismatch $G_i^{(0)}(u, w)$ of subsystem i as a function of vegetation density and soil water, averaged over diurnal and weather cycles under representative semi-arid forcing. The mismatch is positive when energy input exceeds dissipation and negative otherwise. Section 2.2 extends the energy mismatch to a nonlocal functional of u through a gradient expansion.

ASSUMPTION 2.1 (Soil energy mismatch). *The net energy input rate to the soil, $G_1^{(0)}(u, w)$, is a smooth function satisfying three conditions. First, $G_1^{(0)}(0, 0) > 0$: bare dry soil receives more energy than it dissipates. Second, $\partial G_1^{(0)}/\partial u < 0$ for small u : vegetation intercepts incoming radiation, reducing energy input to the soil. Third, $\partial G_1^{(0)}/\partial w < 0$ for small w : increasing soil moisture increases energy dissipation through evaporation.*

TABLE 2

Dimensional model quantities. Signs shown are those assumed in the semi-arid regime of sections 2.1 and 2.3; “free” means the sign depends on the specific ecosystem.

Symbol	Meaning	Sign	Eq.
<i>State variables</i>			
$u(x, t)$	vegetation density (biomass/area)	≥ 0	
$w(x, t)$	soil water content (volume/area)	≥ 0	
<i>Soil energy mismatch $G_1^{(0)}(u, w)$</i>			
a_{00}	net energy input to bare dry soil	> 0	(2.1)
a_{10}	vegetation-induced reduction in soil energy input	> 0	(2.1)
a_{01}	moisture-induced increase in soil energy loss	> 0	(2.1)
<i>Plant energy mismatch $G_2^{(0)}(u, w)$</i>			
γ	canopy energy deficit in the low-density limit	> 0	(2.2)
α_1	energy gain per unit biomass	> 0	(2.2)
α_2	density-dependent energy loss	> 0	(2.2)
β_1	water-dependent cooling	> 0	(2.2)
<i>Spatial interaction (gradient expansion of energy fluxes)</i>			
$\ell_{1,i}$	asymmetric interaction parameter (dim. length)	free	(2.5)
$\ell_{2,i}$	symmetric interaction parameter (dim. length ²)	free	(2.5)
$\ell_{3,i}$	quadratic gradient correction	free	(2.5)
η_1, η_2	spatial coupling functions for G_1, G_2	free	(2.6)–(2.7)
<i>Water loss</i>			
R	rainfall rate	> 0	(2.8)
μ_0	bare-soil evaporation rate	> 0	(2.9)
μ_1	vegetation-induced water loss rate	> 0	(2.9)
<i>Water flux (gradient expansion)</i>			
v_0	bare-soil advection speed	> 0	(2.11)
v_1	vegetation obstruction of flow	> 0	(2.11)
d_0	soil moisture diffusivity	≥ 0	(2.12)
δ_0	vegetation-gradient deflection strength	≥ 0	(2.13)

Taylor expanding around $(u, w) = (0, 0)$,

$$(2.1) \quad G_1^{(0)}(u, w) = a_{00} - a_{10}u - a_{01}w + a_{20}u^2 + a_{11}uw + a_{02}w^2 + \dots$$

where the signs $a_{00}, a_{10}, a_{01} > 0$ are constrained by Theorem 2.1.

ASSUMPTION 2.2 (Plant energy mismatch). *The net energy input rate to the plant canopy, $G_2^{(0)}(u, w)$, is a smooth function satisfying three conditions. First, $\lim_{u \rightarrow 0^+} G_2^{(0)}(u, w) < 0$ for all w : at sufficiently low density, the canopy energy budget is in deficit, because energy capture scales with vegetation density while some dissipative losses persist even at low density. Second, there exists $u_* > 0$ such that $\partial G_2^{(0)}/\partial u > 0$ for $u < u_*$ and $\partial G_2^{(0)}/\partial u < 0$ for $u > u_*$. Since the total incoming energy is bounded, the marginal energy gain per unit vegetation must eventually decrease, so the energy surplus has a single interior maximum. Third, $\partial G_2^{(0)}/\partial w < 0$ for $u > 0$ with $\partial G_2^{(0)}/\partial w|_{u=0} = 0$: water availability enables transpirational cooling, increasing the canopy’s net energy dissipation; this effect vanishes without vegetation.*

The lowest-order polynomial consistent with these constraints is

$$(2.2) \quad G_2^{(0)}(u, w) = -\gamma + \alpha_1 u - \alpha_2 u^2 - \beta_1 uw + \dots$$

where $\gamma, \alpha_1, \alpha_2, \beta_1 > 0$. The signs of $-\gamma$, $+\alpha_1$, and $-\beta_1$ follow directly from the three conditions of Theorem 2.2. The quadratic coefficient $-\alpha_2$ with $\alpha_2 > 0$ is required by

the assumed single maximum: without it, $\partial G_2^{(0)}/\partial u$ would not decrease with u and no interior maximum would exist. Using this low-order polynomial at nonzero steady states is a Taylor approximation, valid when vegetation and water densities are small, as in the semi-arid regime targeted here.

2.2. Spatial structure from gradient expansion. The local energy mismatches $G_i^{(0)}$ depend only on u and w at a single point. In reality, the energy balance at location x depends on the vegetation field in a neighborhood of x , not only on the local values of u and w . As a structural simplification, we let nonlocal dependence enter only through vegetation, with water w entering locally. Nonlocal water-mediated mechanisms such as lateral root water uptake, which the Gilad–Meron framework models explicitly [12], enter our model indirectly through the quasi-steady water functional $W[u]$ developed in section 2.3. Under this simplification, a kernel representation of the spatially extended energy mismatch is, for each subsystem i ,

$$(2.3) \quad G_i[u](x) = \int K_i(x, y, u(x), w(x), u(y)) dy,$$

where K_i is a smooth kernel. We assume this dependence has finite range, so K_i decays on a characteristic interaction length ℓ .

When the interaction range ℓ is short compared to the pattern wavelength λ , the integrand in (2.3) can be Taylor expanded in $u(y)$ about $y = x$. The result is a gradient expansion: a series in spatial derivatives of u with coefficients that depend on the local values of u and w . On a hillslope with a preferred downhill direction along the x -axis, the symmetry $x \rightarrow -x$ is broken, and odd-order derivative terms (such as u_x) are permitted. Truncating at second order in derivatives of u yields

$$(2.4) \quad G_i[u](x) = G_i^{(0)}(u, w) + h_i(u, w) u_x + j_i(u, w) u_{xx} + p_i(u, w) u_x^2 + O(\partial^3),$$

where $G_i^{(0)}$ is the local energy mismatch from section 2.1 and h_i , j_i , p_i are smooth coefficient functions determined by moments of the kernel K_i . Third-order and higher terms are suppressed by powers of ℓ/λ , which is small because interaction ranges are on the order of meters while pattern wavelengths are tens of meters.

The gradient expansion (2.4) introduces three independent coefficient functions for each subsystem. To obtain a tractable minimal model, we impose the following closure: the state dependence of the spatial correction enters through a single amplitude function, while the relative weights of the derivative terms are fixed constants.

ASSUMPTION 2.3 (Effective-density ansatz). *For each subsystem i , the gradient-expansion coefficients in (2.4) factor as*

$$(2.5) \quad h_i = \eta_i(u, w) \ell_{1,i}, \quad j_i = \eta_i(u, w) \ell_{2,i}, \quad p_i = \eta_i(u, w) \ell_{3,i},$$

where $\eta_i(u, w)$ is a smooth function that sets the overall amplitude of the spatial correction at the local state (u, w) . The parameters $\ell_{1,i}$, $\ell_{2,i}$, $\ell_{3,i}$ are constants with dimensions of length, length², and length² per vegetation density.

The factorization assumes that varying the local state rescales the spatial correction without changing its profile. It would be exact for a single dominant interaction kernel with fixed spatial shape and state-dependent amplitude; more generally, it approximates multiple mechanisms by a single effective interaction.

Under Theorem 2.3, the spatially extended energy mismatches become

$$(2.6) \quad G_1 = G_1^{(0)}(u, w) + \eta_1(u, w)(\ell_{1,1} u_x + \ell_{2,1} u_{xx} + \ell_{3,1} u_x^2),$$

$$(2.7) \quad G_2 = G_2^{(0)}(u, w) + \eta_2(u, w)(\ell_{1,2} u_x + \ell_{2,2} u_{xx} + \ell_{3,2} u_x^2).$$

The sign of η_i is not fixed by the general framework; whether the net neighborhood effect amplifies or suppresses the local energy mismatch depends on the ecosystem.

2.3. Water conservation. Water obeys a conservation law:

$$(2.8) \quad \frac{\partial w}{\partial t} = R - L(u, w) - \frac{\partial J}{\partial x},$$

where $R > 0$ is the rainfall rate, $L(u, w) \geq 0$ is the total water loss rate, and J is the spatial water flux; the conservation law is exact. We now constrain L and J using the same approach as for the energy mismatches: smoothness, sign constraints motivated by semi-arid physics, and gradient expansion.

The loss function $L(u, w)$ combines evaporation and transpiration. It is smooth with $\partial L / \partial w > 0$, since water loss increases with available moisture regardless of the specific loss mechanism. The sign of $\partial L / \partial u$ is a regime assumption: vegetation both increases water loss through transpiration and reduces it by shading the soil surface, but in semi-arid systems transpiration dominates, so the net effect is $\partial L / \partial u > 0$. Taylor expanding to leading order gives

$$(2.9) \quad L(u, w) = \mu_0 w + \mu_1 u w + \dots, \quad \mu_0, \mu_1 > 0,$$

where μ_0 is the bare-soil evaporation rate and μ_1 is the vegetation-induced water loss.

For the water flux, the function J at position x depends smoothly on the local values of u , w , and their spatial derivatives. We apply a gradient expansion to first order in derivatives of both u and w :

$$(2.10) \quad J = J_0(u, w) + J_1(u, w) w_x + J_2(u, w) u_x + \dots$$

ASSUMPTION 2.4 (Water flux sign constraints). *The sign constraints below follow from the physics of shallow overland flow, not from ecological arguments. The flux coefficients in (2.10) satisfy the following. The zeroth-order flux $J_0 \geq 0$ with $\partial J_0 / \partial w > 0$, because gravity-driven flux is downhill and increases with water, and $\partial J_0 / \partial u \leq 0$, because stems and litter obstruct shallow flow, increasing surface roughness and reducing overland transport. The diffusive coefficient $J_1 \leq 0$, because water diffuses down its concentration gradient. The deflection coefficient $J_2 \leq 0$ for overland-flow-dominated transport, with $J_2(u, 0) = 0$. Vegetation gradients impede flow through the same roughness mechanism, but deflection requires water to be present.*

As with the energy-mismatch sign constraints, these are regime assumptions appropriate to semi-arid, overland-flow-dominated hillslopes, not universal transport laws. Taylor expanding each coefficient to leading order:

$$(2.11) \quad J_0(u, w) = v_0 w - v_1 u w + \dots, \quad v_0, v_1 > 0,$$

$$(2.12) \quad J_1(u, w) = -d_0 + \dots, \quad d_0 \geq 0,$$

$$(2.13) \quad J_2(u, w) = -\delta_0 w + \dots, \quad \delta_0 \geq 0.$$

The leading terms of J_0 give a vegetation-dependent advective flux $(v_0 - v_1 u)w$, and $J_1 = -d_0$ recovers Fickian diffusion. The J_2 term captures how the water flux responds to vegetation *gradients*: overland flow encountering denser vegetation downstream is impeded by increasing roughness, reducing the net flux in the direction of increasing vegetation density. Section 5 relates this term to existing models.

Water dynamics operate on timescales of hours to days: individual rainfall events last hours, and overland flow redistributes water across hillslope-scale distances within a day. Vegetation dynamics operate on timescales of seasons to decades, set by growth, mortality, and recruitment rates [17]. This timescale separation is standard in dryland vegetation models [12, 16, 19].

ASSUMPTION 2.5 (Timescale separation). *The water field equilibrates to the current vegetation pattern: $\partial w / \partial t \approx 0$, giving*

$$(2.14) \quad 0 = R - L(u, w) - \frac{\partial}{\partial x} [J_0(u, w) + J_1(u, w) w_x + J_2(u, w) u_x].$$

Define $w = W[u](x)$, a nonlocal functional of u .

The functional $W[u]$ is nonlocal: consider the simplified case $d_0 = \delta_0 = 0$, $v_1 = 0$. The quasi-steady equation reduces to the first-order ODE

$$(2.15) \quad v_0 \frac{dw}{dx} = R - (\mu_0 + \mu_1 u) w,$$

which, with $w(0) = 0$ at the hilltop, has the explicit solution

$$(2.16) \quad w(x) = \frac{R}{v_0} \int_0^x \exp\left(-\frac{1}{v_0} \int_y^x (\mu_0 + \mu_1 u(\xi)) d\xi\right) dy.$$

Water at position x is an exponentially weighted integral of upstream rainfall, attenuated by vegetation-dependent losses along the flow path. We retain the diffusion and deflection terms in the full model; they enter the linear stability analysis.

3. Semilinear variational closure and hillslope model. The preceding section developed a constrained class of admissible model ingredients, including sign-constrained energy mismatches, gradient-expansion spatial structure, and quasi-steady water, without specifying the vegetation dynamics. To obtain a concrete PDE, we need an evolution law for the vegetation field that is built from these ingredients. This section defines a family of such closures, selects a distinguished representative on structural grounds, and specializes to a one-dimensional hillslope model.

3.1. A semilinear closure family. The spatially extended energy mismatches G_i from (2.6)–(2.7) depend on u , w , and spatial derivatives of u . The lowest-order tractable coupling is linear in the mismatch and its first two spatial derivatives:

$$(3.1) \quad \frac{\partial u}{\partial t} = f(u, w) + m(u, w) G + n(u, w) G_x - r(u, w) G_{xx},$$

where f , m , n , r are smooth coefficient functions evaluated at the current local state and $w = W[u](x)$ is determined quasi-steadily from (2.14). The minus sign on r is a sign convention whose purpose will become clear in section 4.2, where $r > 0$ combined with the sign of the spatial interaction terms yields a nonpositive quartic coefficient in the dispersion relation and hence short-wavelength regularization. We call this the *semilinear closure family*. All members share the same quasi-steady water coupling

from section 2.3 and the same sign-constrained energy mismatch from section 2.1, so the sign-constrained and gradient-expansion structure is common to the entire family. Section 4 analyzes the linearized consequences: several qualitative features of the dispersion relation hold for any family member, while others are specific to the closure adopted below.

3.2. The Euler–Lagrange representative. We select a distinguished member of the semilinear family (3.1) by choosing a lowest-order score functional and applying the Euler–Lagrange operator at fixed water.

The lowest-order score functional has two components. First, for any smooth local biomass term $\int h(u) dx$ with $h'(0) \neq 0$, the leading nonconstant contribution is proportional to $\int u dx$. The constant $h(0)$ drops out of the Euler–Lagrange operator, and any overall scalar can be absorbed into the relaxation timescale. Thus $\int u dx$ is the universal lowest-order biomass term. Second, for the energy-balance penalty, the lowest-order smooth nonnegative function that vanishes when the energy budget is balanced is G_i^2 . These two lowest-order ingredients give the score functional

$$(3.2) \quad \mathcal{E}[u] = \int_{\Omega} \mathcal{L} dx, \quad \mathcal{L} = u - \frac{\kappa s}{2} [G_1]^2 - \frac{\kappa(1-s)}{2} [G_2]^2,$$

where G_1, G_2 are the spatially extended energy mismatches (2.6)–(2.7), $w = W[u](x)$ is the quasi-steady water field, $s \in [0, 1]$ weights the soil and plant penalties, and $\kappa > 0$ sets the penalty strength relative to the biomass term.

Applying the Euler–Lagrange operator to \mathcal{L} with W treated as an external field, and freezing η at its steady-state value (as discussed below), yields a specific member of the semilinear family:

ASSUMPTION 3.1 (Semilinear variational closure). *The vegetation field evolves according to*

$$(3.3) \quad \frac{\partial u}{\partial t} = \tau \left[\frac{\partial \mathcal{L}}{\partial u} - \frac{d}{dx} \frac{\partial \mathcal{L}}{\partial u_x} + \frac{d^2}{dx^2} \frac{\partial \mathcal{L}}{\partial u_{xx}} \right]_{W=W[u]},$$

where \mathcal{L} is the Lagrangian density from (3.2), $\tau > 0$ is a relaxation rate, and $W[u]$ is determined quasi-steadily at each instant from the water conservation equation.

With η frozen at a constant value, the Euler–Lagrange operator at fixed W maps the score functional to specific coefficient functions (f, m, n, r) in (3.1). Water enters independently through its own quasi-steady conservation law. The coupled vegetation–water system is therefore not a single-field gradient flow; this distinction is essential, because a single-field gradient flow would have self-adjoint linearization and hence real spectrum, precluding traveling modes.

Within the semilinear family, the Euler–Lagrange choice is distinguished by algebraic structure. It forces the local dispersion symbol to be even in wavenumber and the quartic coefficient to be nonpositive. As shown in section 4.2, when the asymmetric interaction length is nonzero this evenness determines the closure coefficients up to a positive rescaling absorbed into τ , making the EL representative essentially unique. The nonpositive quartic then gives short-wavelength regularization without parameter tuning. Evenness also implies that all odd-in- k contributions enter through the water coupling, so band migration is driven entirely by the water-mediated part of the dynamics.

Because G_i contains u_{xx} from the gradient expansion, the Euler–Lagrange term $d^2/dx^2(\partial \mathcal{L}/\partial u_{xx})$ produces fourth-order spatial derivatives. These provide short-

wavelength regularization and wavelength selection, as in the Swift–Hohenberg equation [22], but here arising from the variational closure rather than being postulated.

We now specialize minimally to $s = 0$, retaining only the plant energy mismatch G_2 . This is the simplest single-subsystem representative of the closure. G_2 contains the richer nonlinear structure, including the sign change in $\partial G_2/\partial u$ and the water-coupling term $\beta_1 u w$, whereas G_1 is linear in u to leading order. Setting $s = 0$ removes G_1 from the vegetation dynamics entirely; the soil energy balance influences vegetation only indirectly, through the physical processes (evaporation, transpiration) that determine the quasi-steady water field. We leave the case $s > 0$ to future work.

With $s = 0$, the energy penalty involves only G_2 , and the spatial correction function $\eta_2(u, w)$ from (2.7) is the only one that enters. We write η_2 simply as η . We impose an additional closure and freeze the spatial coupling amplitude at its reference-state value, $\eta = \eta(U_0, W_0)$. Ecologically, this amounts to treating the effective strength of neighborhood energetic interactions as slowly varying near the reference state, consistent with the effective-density ansatz (Theorem 2.3) that already fixes the spatial profile shape. We analyze the quantitative effect of this closure on the dispersion relation in section 4.2. It shifts the quadratic coefficient D by an asymptotically small amount in the weak-penalty regime while preserving the qualitative structure: even parity and nonpositive quartic. We therefore analyze the frozen- η representative closure below.

We also write $\ell_{1,2}$ and $\ell_{2,2}$ as ℓ_1 and ℓ_2 , dropping the subsystem index since only the plant parameters appear. The plant energy mismatch including spatial corrections is then

$$(3.4) \quad G_2 = -\gamma + \alpha_1 u - \alpha_2 u^2 - \beta_1 u w + \eta(\ell_1 u_x + \ell_2 u_{xx}),$$

with $\gamma, \alpha_1, \alpha_2, \beta_1 > 0$ and $w = W[u](x)$ from the quasi-steady water equation. We set $\ell_3 = 0$ throughout. Since the term $\ell_3 u_x^2$ does not contribute at linear order, this omission does not affect the linear stability analysis; beyond linear order it is a simplifying closure choice. The Lagrangian becomes $\mathcal{L} = u - (\kappa/2)G_2^2$.

We nondimensionalize using scales derived from the model coefficients: $u_* = \alpha_1/(2\alpha_2)$ is the peak of the water-independent quadratic $\alpha_1 u - \alpha_2 u^2$ in G_2 ; $w_* = \alpha_1/\beta_1$ is the water content at which the w -dependent cooling term balances the energy gain at density u_* ; $x_* = v_0/\mu_0$ is the downstream distance over which bare-soil water loss depletes the water column; and we choose t_* to normalize the nondimensional Lagrangian. Explicitly:

$$(3.5) \quad u_* = \frac{\alpha_1}{2\alpha_2}, \quad w_* = \frac{\alpha_1}{\beta_1}, \quad x_* = \frac{v_0}{\mu_0}, \quad G_* = \alpha_1 u_* = \frac{\alpha_1^2}{2\alpha_2}, \quad t_* = \frac{u_*^2}{\tau \kappa G_*^2},$$

where G_* is a characteristic scale for the dimensional energy mismatch. We define dimensionless variables $U = u/u_*$, $W = w/w_*$, $X = x/x_*$, $T = t/t_*$. With this choice, the nondimensional Lagrangian density takes the form $\mathcal{L} = \mu U - \frac{1}{2}G^2$, where $G = G_2/G_*$ is the dimensionless energy mismatch and

$$(3.6) \quad \mu = \frac{u_*}{\kappa G_*^2} = \frac{2\alpha_2}{\kappa \alpha_1^3}$$

is a dimensionless parameter measuring the relative strength of the biomass drive

versus the energy-balance penalty. The dimensionless parameters are

$$(3.7) \quad \begin{aligned} \Gamma &= \frac{\gamma}{G_*}, & \rho &= \frac{R}{\mu_0 w_*}, & \beta &= \frac{\mu_1 u_*}{\mu_0}, & \Lambda_1 &= \frac{\ell_1}{x_*}, \\ \Lambda_2 &= \frac{\ell_2}{x_*^2}, & \mathcal{D} &= \frac{d_0}{v_0 x_*}, & \Delta &= \frac{\delta_0 u_*}{v_0 x_*}, & \chi &= \frac{v_1 u_*}{v_0}. \end{aligned}$$

TABLE 3

Dimensionless parameters. Most are formed from the dimensional quantities in Table 2 and the nondimensionalization scales (3.5); ν denotes the hillslope-advection setting.

Symbol	Meaning	Definition
μ	biomass drive vs. energy penalty	$u_*/(\kappa G_*^2) = 2\alpha_2/(\kappa\alpha_1^3)$
Γ	energy deficit at zero vegetation	γ/G_*
ρ	dimensionless rainfall	$R/(\mu_0 w_*)$
β	vegetation-dependent water loss	$\mu_1 u_*/\mu_0$
Λ_1	asymmetric interaction length	ℓ_1/x_*
Λ_2	symmetric interaction length	ℓ_2/x_*^2
\mathcal{D}	soil moisture diffusivity	$d_0/(v_0 x_*)$
Δ	vegetation-gradient deflection	$\delta_0 u_*/(v_0 x_*)$
χ	vegetation obstruction of overland flow	$v_1 u_*/v_0$
η	spatial correction amplitude (at steady state)	$\eta_2(U_0, W_0) u_*/G_*$
ν	hillslope advection speed	1 on slope; 0 on flat terrain
U_0	uniform steady-state vegetation	from (4.3)
W_0	uniform steady-state water	$\rho/(1 + \beta U_0)$
G_0	energy mismatch at steady state	$-\Gamma + U_0 - \frac{1}{2}U_0^2 - U_0 W_0$

In dimensionless form, $G_2/G_* = G$; we give the explicit expression for G when we collect the full model below in (3.9). After nondimensionalization, we reuse the symbol η for the corresponding dimensionless frozen amplitude (see Table 3). The sign of η is not fixed by the energy-balance arguments of section 2; it depends on whether the net neighborhood effect at steady-state density U_0 is amplifying or suppressing. For the instability analysis below, we take $\eta > 0$, corresponding to a regime in which the net neighborhood effect enhances the local energy mismatch at the relevant density scale. When $\eta < 0$, the instability conditions change qualitatively, as discussed in section 4.

The complete dimensionless model is as follows. Evaluating the Euler–Lagrange operator on $\mathcal{L} = \mu U - \frac{1}{2}G^2$ with η frozen at its steady-state value, the vegetation equation becomes

$$(3.8) \quad \frac{\partial U}{\partial T} = \mu - G q_G + \eta \Lambda_1 G_X - \eta \Lambda_2 G_{XX},$$

where $q_G = 1 - U - W$ is the partial derivative $\partial G/\partial U$ at fixed W ; at the uniform steady state this reduces to the constant $q = 1 - U_0 - W_0$ used in section 4. The quantities G_X and G_{XX} are the spatial derivatives of the energy mismatch

$$(3.9) \quad G = -\Gamma + U - \frac{1}{2}U^2 - UW + \eta(\Lambda_1 U_X + \Lambda_2 U_{XX}).$$

The water field W is determined quasi-steadily by

$$(3.10) \quad \frac{\partial}{\partial X} [\nu(1 - \chi U) W - \mathcal{D} W_X - \Delta W U_X] = \rho - (1 + \beta U) W,$$

where ν is the dimensionless hillslope advection speed (1 on a slope, 0 on flat terrain; in the flat case, we retain x_* as a fixed reference length scale derived from

the slope regime). The $(1 - \chi U)$ factor captures the reduction of overland flow by denser vegetation. The linear stability analysis and numerical simulations below use a spatially periodic domain, representing a local patch of a long hillslope far from the boundaries. Table 3 defines all dimensionless parameters; Table 4 lists their baseline values for numerical simulations. The model (3.8)–(3.10) is one specific member of the semilinear closure family (3.1), selected by the Euler–Lagrange closure and the further specializations $s = 0$, frozen η , and $\ell_3 = 0$. The analysis that follows should be read as properties of this representative closure, not as universal consequences of the framework.

4. Linear stability analysis. We now ask whether the uniform vegetated state derived in sections 2 and 3 is stable to spatially periodic perturbations. We compute the uniform steady state, linearize the vegetation–water system in Fourier space, and, for the Euler–Lagrange representative, obtain an exact decomposition of the growth rate into a local even polynomial and a water-coupling contribution. We identify three physically distinct instability mechanisms within this structure.

4.1. Uniform steady state. With all spatial derivatives zero, the water equation gives

$$(4.1) \quad W_0 = \frac{\rho}{1 + \beta U_0}.$$

For the vegetation, the Euler–Lagrange operator (3.8) at the uniform state treats W as an external field; the spatial derivative terms G_X and G_{XX} vanish, leaving $\mu - G_0 q$, where

$$(4.2) \quad q = \left. \frac{\partial G}{\partial U} \right|_W = 1 - U_0 - W_0$$

is the partial derivative of the energy mismatch with respect to vegetation at fixed water. Setting the right-hand side to zero gives the steady-state condition

$$(4.3) \quad \mu = G_0 q,$$

where $G_0 \equiv G(U_0, W_0) = -\Gamma + U_0 - \frac{1}{2}U_0^2 - U_0W_0$. Together with $W_0 = \rho/(1 + \beta U_0)$, this implicitly determines $U_0(\mu, \Gamma, \rho, \beta)$.

The steady-state equation may admit multiple positive roots. The linearization formulas below apply to any homogeneous branch (U_0, W_0) satisfying (4.3); different branches generally produce different coefficient values and hence potentially different stability behavior. The onset-oriented analysis evaluates them on the lower vegetated branch, which connects continuously to the pattern-onset regime as rainfall increases from zero. Other questions, such as collapse from well-established vegetation, may require analyzing the upper branch or both branches. At the parameter values used in section 6, μ is small and $G_0 > 0$ on this branch.

4.2. Perturbation and dispersion relation. We perturb the uniform state and linearize:

$$(4.4) \quad U = U_0 + \epsilon \tilde{U}, \quad W = W_0 + \epsilon \tilde{W}, \quad \tilde{U} = \hat{U} e^{ikX + \sigma T},$$

where σ is the dimensionless growth rate.

Linearizing the quasi-steady water equation (3.10) and solving for the water response to a vegetation perturbation at wavenumber k gives the water transfer function

(derivation in A):

$$(4.5) \quad \hat{W} = \Phi(k)\hat{U}, \quad \Phi(k) = \frac{-W_0(\beta + \Delta k^2 - i\chi\nu k)}{1 + \beta U_0 + \mathcal{D}k^2 + ic_0k},$$

where $c_0 = \nu(1 - \chi U_0)$ is the effective advection speed at the steady state.

The water transfer function $\Phi(k)$ depends only on the quasi-steady water equation and is therefore common to every member of the semilinear closure family (3.1). For any member of that family, linearizing the vegetation equation and substituting $\delta W = \Phi(k)\delta U$ yields a dispersion relation of the form

$$(4.6) \quad \sigma(k) = \mathcal{A}(k) + \mathcal{B}(k)\Phi(k),$$

where $\mathcal{A}(k)$ is the local contribution from the vegetation equation at fixed water and $\mathcal{B}(k)\Phi(k)$ is the water-coupling contribution. This decomposition holds regardless of which coefficient functions f , m , n , r are chosen: it is a consequence of the semilinear architecture, not of the specific closure.

What is *not* guaranteed at the family level is the detailed structure of $\mathcal{A}(k)$. Because the gradient expansion of G includes the asymmetric first-derivative term $\eta\Lambda_1 U_X$, a general member of the closure family can have odd-in- k contributions in the local part. Neither the evenness of $\mathcal{A}(k)$ nor the sign of its highest-order coefficient is a family-level property; both depend on the specific closure.

For the Euler–Lagrange representative (3.3), the variational structure forces additional algebraic constraints. To see why, note that the family equation (3.1) couples the closure operator (with coefficients m , n , r) to the energy mismatch G . Linearizing at the uniform state and Fourier transforming, the local part of $\sigma(k)$ (at fixed water) becomes a k -independent contribution plus a product of two Fourier symbols. The first, $M(k) = m_0 + ikn_0 + r_0k^2$, is the symbol of the closure operator evaluated at the steady state. The second, $P(k) = q + ik a_0 - b_0k^2$, is the symbol of the mismatch G linearized in U , where $q = 1 - U_0 - W_0$, $a_0 = \eta\Lambda_1$, and $b_0 = \eta\Lambda_2$. For the EL closure, the coefficient functions satisfy $m_0 = -q$, $n_0 = a_0$, and $r_0 = b_0$, so the real parts of $M(k)$ and $P(k)$ are exact opposites while the imaginary (first-derivative) parts are identical. Expanding the product $M(k)P(k)$, all odd-in- k terms cancel, and the general local symbol $\mathcal{A}(k)$ reduces to a real even polynomial that we write as

$$(4.7) \quad \mathcal{A}(k) = A + Dk^2 + Ek^4.$$

As shown in C, the state dependence of η contributes an additional even k^2 term, $2G_0\eta_{0,U}\Lambda_2$ (where $\eta_{0,U} = \partial\eta/\partial U$ at the steady state), to the local symbol. Freezing η sets this correction to zero. In the weak-penalty regime, $G_0 = \mu/q$ is small on the lower vegetated branch, so if η varies on an $O(1)$ state scale this correction is asymptotically smaller than the retained $2\eta_0\Lambda_2q$ term in D . The frozen- η closure therefore shifts D quantitatively but preserves the even parity, the nonpositive quartic, and the fact that all odd-in- k terms arise through water coupling.

The coefficients are

$$(4.8) \quad A = -q^2 + G_0, \quad D = 2\eta\Lambda_2q - \eta^2\Lambda_1^2, \quad E = -\eta^2\Lambda_2^2.$$

The quartic coefficient satisfies $E \leq 0$, with equality only when $\eta\Lambda_2 = 0$, guaranteeing short-wavelength regularization. This is a direct consequence of the variational pairing: the Euler–Lagrange operator uses the same second-derivative structure as G , forcing the quartic coefficient to be a negative square. A different member of the

closure family (3.1) could have $E > 0$ or could have odd-in- k local contributions; neither occurs in the EL representative.

When $a_0 = \eta\Lambda_1 \neq 0$ (the slope regime), evenness essentially determines the closure: it pins down the linearized derivative coefficients up to a single scalar. To see this, consider a general family member with local symbol $M(k)P(k)$, where $M(k) = m_0 + in_0k + r_0k^2$ and $P(k) = q + ia_0k - b_0k^2$. Requiring $M(k)P(k)$ to be even in k forces the odd coefficients to vanish:

$$(4.9) \quad m_0a_0 + n_0q = 0, \quad -n_0b_0 + r_0a_0 = 0.$$

Setting $c = n_0/a_0$, these give $m_0 = -cq$, $n_0 = ca_0$, $r_0 = cb_0$ for a single scalar c . The EL closure corresponds to $c = 1$; any $c > 0$ can be absorbed into the relaxation rate τ . For any such closure, the quartic coefficient is $E = -cb_0^2 = -c\eta^2\Lambda_2^2 \leq 0$ —the nonpositive quartic is a consequence of evenness, not an independent condition. Up to the choice of relaxation rate, the EL representative is therefore the unique member of the semilinear family whose linearized derivative coefficients (m_0, n_0, r_0) produce an even local symbol in the slope regime $\Lambda_1 \neq 0$. When $\Lambda_1 = 0$, the mismatch $P(k)$ is already even, so evenness of $M(k)P(k)$ constrains only $n_0 = 0$, leaving m_0 and r_0 free. The EL closure remains a natural choice in this regime but is no longer uniquely selected by evenness alone.

Because $\mathcal{A}(k)$ is even, all odd-in- k contributions to $\sigma(k)$ enter through the water coupling $\mathcal{B}(k)\Phi(k)$. Band migration is therefore driven entirely by the water response on the hillslope, not by Λ_1 acting through the local energy functional. The parameter Λ_1 enters the local part only through even powers of k , modifying the balance between destabilizing and stabilizing contributions. This too is a consequence of the EL closure, not a family-level fact.

The water perturbation $\delta W = \Phi(k)\delta U$ feeds back through the $-UW$ term in G . Because the Euler–Lagrange operator has spatial derivatives acting on water-dependent terms, the coefficient multiplying $\Phi(k)$ is itself k -dependent:

$$(4.10) \quad \mathcal{B}(k) = B_0 + B_1(ik) + B_2k^2,$$

where

$$(4.11) \quad B_0 = qU_0 + G_0, \quad B_1 = -\eta\Lambda_1 U_0, \quad B_2 = -\eta\Lambda_2 U_0.$$

Here B_0 is the uniform ($k = 0$) water–vegetation coupling strength, while B_1 and B_2 describe how the Euler–Lagrange spatial operators modulate the coupling at finite wavenumber. Combining (4.6), (4.7), and (4.10), the exact dispersion relation for the EL closure is

$$(4.12) \quad \sigma(k) = A + Dk^2 + Ek^4 + \mathcal{B}(k)\Phi(k),$$

an exact decomposition into a local even polynomial and a water-coupling contribution. The sign and magnitude of D depend on the balance between $2\eta\Lambda_2q$ (state-dependent, through q) and $\eta^2\Lambda_1^2$ (state-independent). In the regime studied here, $\eta > 0$, $\Lambda_2 > 0$, and $q > 0$, so the first term is positive and promotes finite-wavenumber instability, while the second is a stabilizing correction from the slope.

The three instability mechanisms correspond to distinct contributions within this structure: energy-balance spatial coupling through Dk^2 , water-mediated feedback through $\mathcal{B}(k)\Phi(k)$, and water deflection by vegetation gradients through the Δ -dependence of $\Phi(k)$. The quartic term Ek^4 provides the stabilizing short-wavelength

cutoff. Section 4.3 analyzes each mechanism. Figure 1 illustrates this decomposition in the $\Lambda_1 = 0$ regime for two values of the interaction length Λ_2 , showing how the energy-balance spatial coupling influences the selected wavenumber.

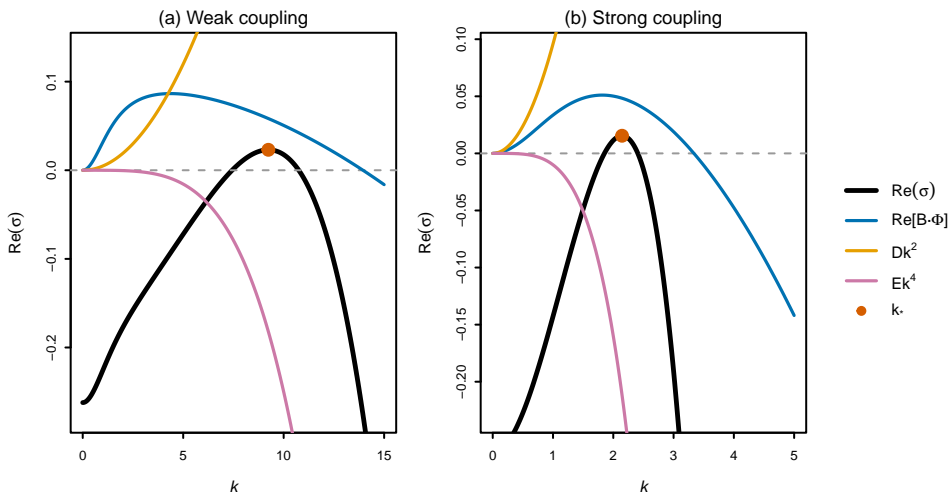


FIG. 1. Dispersion relation $\text{Re}[\sigma(k)]$ (black) and the k -dependent increments of each term in the decomposition (4.12), relative to $k = 0$: water-coupling increment $\text{Re}[\mathcal{B}(k)\Phi(k)] - \text{Re}[\mathcal{B}(0)\Phi(0)]$ (blue), energy-balance spatial coupling Dk^2 (orange), and fourth-order cutoff Ek^4 (pink). Filled circles mark the most unstable wavenumber k_* . Both panels use $\Lambda_1 = 0$ and $\Delta = 0$ with other parameters at baseline values from Table 4, including $\nu = 1$. (a) Weak spatial coupling ($\Lambda_2 = 0.005$): $k_* \approx 9.8$, $\sigma_{\max} \approx 0.010$. (b) Strong energy-balance coupling ($\Lambda_2 = 0.1$): the larger interaction length shifts k_* down to ≈ 2.2 and selects a longer wavelength, consistent with (4.15). These panels use an illustrative regime with $\Lambda_1 = 0$ (suppressing asymmetric energy interactions while retaining water advection), where the local polynomial is the primary determinant of the selected wavenumber. Note the different k -axis range in (b).

4.3. Instability mechanisms. From (4.12), the real part of the dispersion relation is

$$(4.13) \quad \text{Re}[\sigma(k)] = A + Dk^2 + Ek^4 + \text{Re}[\mathcal{B}(k)\Phi(k)].$$

Writing $p = 1 + \beta U_0 + \mathcal{D}k^2$ (where \mathcal{D} is the soil moisture diffusivity from (3.10)) and $c_0 = \nu(1 - \chi U_0)$,

$$(4.14) \quad \text{Re}[\Phi(k)] = \frac{-W_0[(\beta + \Delta k^2)p - \chi \nu c_0 k^2]}{p^2 + c_0^2 k^2}.$$

The $-\chi \nu c_0 k^2$ correction in the numerator is the finite-wavenumber contribution from vegetation obstruction. It reduces the magnitude of the negative water coupling at intermediate k . Because c_0 depends on rainfall through U_0 , this correction also provides a rainfall-dependent contribution to wavelength selection.

Pattern formation requires three conditions. First, the uniform state must be stable at $k = 0$: $\sigma(0) = A + B_0 \Phi(0) < 0$. Second, it must be unstable at some finite wavenumber $k_* > 0$: $\text{Re}[\sigma(k_*)] > 0$. Third, it must be restabilized at large k . Whenever $\eta \Lambda_2 \neq 0$, the quartic coefficient $E = -\eta^2 \Lambda_2^2 < 0$ guarantees this.

Three mechanisms can drive the instability at intermediate k . The first is the *water-mediated feedback*, operating through $\text{Re}[\mathcal{B}(k)\Phi(k)]$: a vegetation perturbation modifies the local water balance, altering water availability for neighboring

vegetation and feeding back into the energy balance. The mechanism is classical and structurally analogous to the Klausmeier instability. The coupling strength is wavenumber-dependent through $\mathcal{B}(k)$; the β term in the numerator of $\Phi(k)$ provides the k -independent baseline of the water response.

The second is the *energy-balance spatial coupling*, which operates through the Dk^2 term in the dispersion relation. When $D > 0$, the linearized Euler–Lagrange operator acting on spatial perturbations is less stabilizing at finite wavenumber than at $k = 0$. This makes the uniform state easier to destabilize. Although standard models also contain k^2 terms, this contribution arises from the variational closure of the gradient-expanded energy functional rather than from explicit water feedback, and the interaction lengths determine its coefficient through the Euler–Lagrange linearization. In the illustrative regime $\Lambda_1 = 0$ with $\eta > 0$ and $q > 0$, $D = 2\eta\Lambda_2q > 0$ and this mechanism can drive finite-wavenumber instability even when the water-coupling terms $\mathcal{B}(k)\Phi(k)$ are weak. On slopes ($\Lambda_1 > 0$), the $-\eta^2\Lambda_1^2$ contribution reduces D , and the role of the local variational terms shifts from driving the instability to providing stabilizing regularization. The water-mediated coupling then takes on the primary role in determining the instability band.

The third, *water deflection by vegetation gradients*, operates through the Δk^2 term in the numerator of $\Phi(k)$. Vegetation gradients deflect overland flow, strengthening the coupling at finite k relative to $k = 0$. This mechanism is absent from standard dryland vegetation models.

Band migration arises from $\text{Im}[\sigma(k)]$, entirely from water coupling $\mathcal{B}(k)\Phi(k)$. Three sources contribute odd-in- k terms: the advective ik in $\Phi(k)$'s denominator when $\nu \neq 0$, the $-i\chi\nu k$ term in $\Phi(k)$'s numerator when $\nu \neq 0$, and the $B_1(ik)$ factor when $\Lambda_1 \neq 0$. On flat terrain, all three sources vanish: $\nu = 0$ eliminates both numerator and denominator contributions to Φ , and in the physical flat-terrain regime $\Lambda_1 = 0$ as well, so $B_1 = 0$. Migration therefore vanishes on flat terrain, consistent with field observations. Band migration is thus associated with directional water flow rather than the local polynomial, though the energy budget enters indirectly through $B_1 = -\eta\Lambda_1U_0$, which modulates the water-coupling strength.

To illustrate the role of the local polynomial, consider the regime $D > 0$ with weak water coupling. The most unstable wavenumber of $A + Dk^2 + Ek^4$ simplifies to

$$(4.15) \quad k_* \approx \sqrt{\frac{D}{2|E|}} = \sqrt{\frac{2\eta\Lambda_2q - \eta^2\Lambda_1^2}{2\eta^2\Lambda_2^2}},$$

giving dimensional wavelength $\lambda_* = 2\pi x_*/k_*$. In the baseline parameter regime, $q = 1 - U_0 - W_0 > 0$ on the lower vegetated branch, and q increases as rainfall ρ decreases. This local-polynomial prediction therefore gives k_* increasing with aridity—the *wrong* sign relative to the empirical observation that pattern wavelength increases with aridity [8].

On sloped terrain, the physically relevant regime has $\Lambda_1 > 0$, reflecting the $x \rightarrow -x$ asymmetry of the hillslope in the gradient expansion. In this regime, $D = 2\eta\Lambda_2q - \eta^2\Lambda_1^2$ is reduced and can become negative, so the local polynomial no longer supports a finite-wavenumber instability on its own. The water-mediated term $\mathcal{B}(k)\Phi(k)$ then becomes the primary driver of wavelength selection. The shape and peak location of $\text{Re}[\Phi(k)]$ depend on rainfall through U_0 and W_0 . As rainfall decreases, the most unstable wavenumber shifts to lower values, corresponding to longer wavelengths. Consequently, the full dispersion relation produces the empirically correct rainfall–

wavelength trend in this regime. Numerical evaluation of the full $\text{Re}[\sigma(k)]$ across the instability window confirms this: at baseline parameters with $\Lambda_1 \gtrsim 0.05$, we find that $\lambda_*(\rho)$ decreases monotonically with ρ , consistent with Deblauwe et al. [8]. Section 6.1 analyzes this regime in detail. When deflection is significant ($\Delta > 0$), the Δk^2 term in the numerator of $\Phi(k)$ further enhances the water coupling at finite k relative to $k = 0$, shifting k_* to larger values in the regimes studied here.

To map the relative importance of these mechanisms, we compute a classification in the illustrative regime $\Lambda_1 = 0$, $\nu = 1$, where both mechanisms can contribute and neither is suppressed by symmetry. We compare the full dispersion relation against two reductions: a “no kernel” model ($\eta = 0$, removing energy-balance spatial coupling) and a “no water” model ($\beta = \chi = \Delta = 0$, removing all vegetation–water coupling). A mechanism is necessary at a given parameter point if removing it eliminates the finite-wavenumber instability. Figure 2 shows this classification across two parameter planes: (ρ, Γ) and (ρ, β) . Energy-balance coupling alone can drive instability; water-mediated feedback alone can drive instability; both act synergistically; in the (ρ, Γ) plane, a small region allows either mechanism alone. Setting $\beta = \chi = \Delta = 0$ changes the steady state itself, since $W_0 = \rho/(1 + \beta U_0)$ depends on β , so the comparison does not isolate the effect of the coupling alone. The classification therefore identifies necessary structural components, not independent causal contributions. Setting $\eta = 0$, by contrast, does not alter the uniform steady state, since η enters only through spatial derivative terms that vanish at the homogeneous solution.

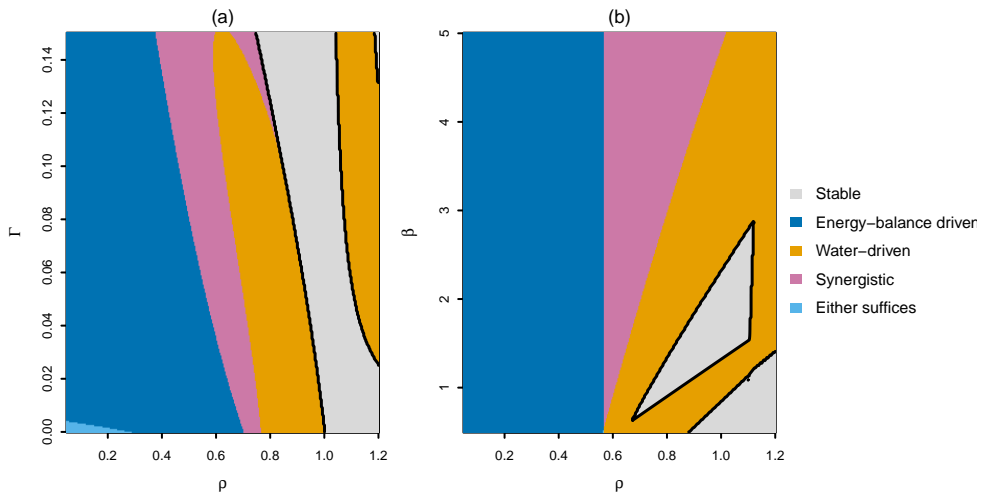


FIG. 2. Mechanism classification across parameter space. At each point, the full dispersion relation and two reductions—no energy-balance spatial coupling ($\eta = 0$) and no water-mediated feedback ($\beta = \chi = \Delta = 0$)—are evaluated; a mechanism is necessary if removing it eliminates the instability. (a) (ρ, Γ) plane. (b) (ρ, β) plane. Colors: energy-balance driven (blue), water driven (orange), synergistic (pink), either suffices (light blue), stable (gray). Black contour marks the linear stability boundary. Computed at $\Lambda_1 = 0$ with $\nu = 1$ and other parameters at baseline values (Table 4) unless varied on the axes. This is an illustrative mathematical regime that suppresses the asymmetric energy interaction while retaining water advection; the physical flat-terrain limit is $\Lambda_1 = 0$, $\nu = 0$.

The preceding analysis assumes that the quasi-steady water equation remains well-posed as patterns grow, meaning its zeroth-order coefficient stays positive everywhere. We develop heuristic admissibility constraints on the vegetation obstruction

strength χ in F to ensure this condition holds, and we verify them at the baseline parameter values in section 6.

5. Comparison with existing models. A structural comparison with the Klausmeier model (1.1), detailed in E, highlights several differences. The $\beta_1 uw$ term in our model plays the same structural role as the Klausmeier uptake wn^2 ; the different power of n reflects different density-dependence assumptions. Both forms are consistent with the sign constraints from Theorem 2.2. Water advection and diffusion appear in both models, but in our framework they emerge from the gradient expansion rather than being postulated independently. Rietkerk et al. [19] introduced separate compartments for overland flow and soil moisture; our single-flux gradient expansion sidesteps this distinction. The Klausmeier model includes $D_n \nabla^2 n$ as postulated plant dispersal; our second-order spatial terms instead reflect the finite range of plant–plant interactions entering through the energy mismatch. Wavelength selection differs correspondingly: the Klausmeier selected wavenumber depends on the interaction of reaction terms with plant diffusion, while ours involves the fourth-order cutoff Ek^4 with $E = -\eta^2 \Lambda_2^2$.

In the illustrative regime $\Lambda_1 = 0$ where the local polynomial controls selection (section 4.3), the wavelength scaling $\lambda_* \sim \Lambda_2^{1/2}$ differs from the Klausmeier scaling, reflecting the different cutoffs (k^4 versus k^2). On slopes where the water coupling dominates, the wavelength is instead set by the water transfer function $\Phi(k)$ and the variational cutoff Ek^4 . The normalized dispersion curves (E) show a further contrast: our model produces a narrow Turing-type instability band, while the Klausmeier model has a broad dome at representative parameter values. A narrow band constrains the selected wavelength tightly; a broad band permits greater variability in the realized pattern.

The comparison with the Gilad–Meron framework raises a different question. The three-feedback framework of Gilad et al. [11, 12]—infiltration, water uptake with root augmentation, and shading—has become an organizing principle in the field [17, 18].

Our model also identifies three instability mechanisms, but the decomposition differs in kind. In the Gilad–Meron framework, all three feedbacks are water-mediated: they describe different spatial pathways by which vegetation and water interact. Their shading feedback is physically related to the energy-balance considerations in our framework, even though it enters their equations differently. Our claim concerns how the mechanisms appear in the dispersion relation, not that earlier authors ignored energy-balance effects. In our framework, the exact dispersion relation (4.12) separates into a local even polynomial and a water-coupling contribution. This structure identifies three mechanisms: energy-balance spatial coupling (Dk^2) from the local part, and water-mediated feedback and deflection (through Δk^2 in $\Phi(k)$) from the water-coupling term $\mathcal{B}(k)\Phi(k)$.

The energy-balance spatial coupling does not appear in this separable form in the Klausmeier, Rietkerk, or Gilad–Meron-type formulations discussed here. When $\Lambda_1 = 0$ and $D > 0$, the Dk^2 term can drive finite-wavenumber instability even when the water-coupling terms $\mathcal{B}(k)\Phi(k)$ are weak. This identifies a structurally distinct instability pathway rooted in the local energy-balance part of the linearized operator. On slopes, the asymmetric interaction reduces D and the energy-balance spatial coupling acts primarily as a stabilizing regularization. The water-mediated term then takes the leading role in wavelength selection and produces the correct rainfall–wavelength trend.

The water deflection mechanism ($J_2 u_x = -\delta_0 w u_x$) is related to, but distinct

from, the infiltration feedback of Gilad et al. [12]. Both describe how vegetation spatial structure modulates water transport. However, the infiltration feedback represents a specific biocrust-mediated mechanism through a postulated functional form. Our deflection term is instead a coarse-grained gradient-expansion coefficient that represents the net effect of vegetation gradients on overland flow without specifying a particular physical mechanism.

6. Numerical simulations. We solve the nonlinear system numerically to test whether the linear predictions survive into the finite-amplitude regime and to explore the nonlinear branch structure. We use pseudospectral spatial discretization [5] on a periodic domain with ETDRK4 time integration [6, 15]; full details of the numerical scheme are given in G. Table 4 collects all baseline parameter values; individual figures vary one or more parameters as noted in their captions.

TABLE 4
Baseline parameter values for numerical simulations.

Symbol	Meaning	Baseline value
Γ	energy deficit at zero vegetation	0.05
ρ	dimensionless rainfall	0.5
β	vegetation-dependent water loss	2.0
Λ_1	asymmetric interaction length	0.10 ($\Lambda_1 > 0$); 0 ($\Lambda_1 = 0$)
Λ_2	symmetric interaction length	0.01
\mathcal{D}	soil moisture diffusivity	0.01
Δ	vegetation-gradient deflection	0.10
χ	vegetation obstruction of flow	2.0
η	spatial coupling amplitude	1.0
μ	biomass drive vs. energy penalty	0.005
ν	hillslope advection speed	1 (slope); 0 (flat)

These values are illustrative, not calibrated to a specific ecosystem; our aim is to exhibit the qualitative behavior the energy-balance closure produces. We choose them to place the model in the regime analyzed in sections 3 and 4: weak energy penalty ($\mu \ll 1$), nonzero slope ($\Lambda_1 > 0$) for the slope-regime results, and order-one water coupling (β, ρ) so that neither the vegetation nor water dynamics is negligible.

As noted in section 4.3, the linear analysis requires the quasi-steady water equation to remain well-posed, meaning its zeroth-order coefficient $b(X) = 1 + \beta U - \nu \chi U_X - \Delta U_{XX}$ stays positive everywhere. At the baseline steady state with $\rho = 0.5$ on the lower vegetated branch, $U_0 \approx 0.11$ and the flow-reduction factor is $1 - \chi U_0 \approx 0.78$; the value $\chi = 2$ satisfies both admissibility constraints from F at all computed parameter values.

6.1. Wavelength selection and rainfall dependence. On sloped terrain with $\Lambda_1 > 0$, the linear theory predicts that as rainfall ρ decreases, the most unstable wavelength $\lambda_* = 2\pi/k_*$ increases—patterns become coarser in more arid conditions (the Deblauwe trend [8]). As described in section 4.3, the asymmetric interaction reduces D and the water-mediated coupling becomes the primary driver of wavelength selection, shifting the instability peak to lower wavenumbers under drier conditions. To test whether this prediction survives in the full nonlinear dynamics, we sweep ρ across the instability window with $\Lambda_1 = 0.10$ and compare the dominant wavelength from nonlinear simulations against the linear prediction. All simulations share a common domain length $L = 20 \lambda_*(\rho_{\text{mid}})$, where ρ_{mid} is the median rainfall in the sweep, and integrate to $T_{\text{end}} = 1000$.

Figure 3 shows the results. Panel (a) plots λ_* versus ρ over the upper portion of the instability window. The linear theory curve, box-quantized admissible wavelengths L/n in the finite periodic domain, and nonlinear simulation points agree well across the computed range. Panel (b) shows the dispersion relation $\text{Re}[\sigma(k)]$ at four rainfall values. In the slope regime, the most unstable wavenumber k_* increases with ρ (shorter wavelength at higher rainfall), consistent with the Deblauwe trend.

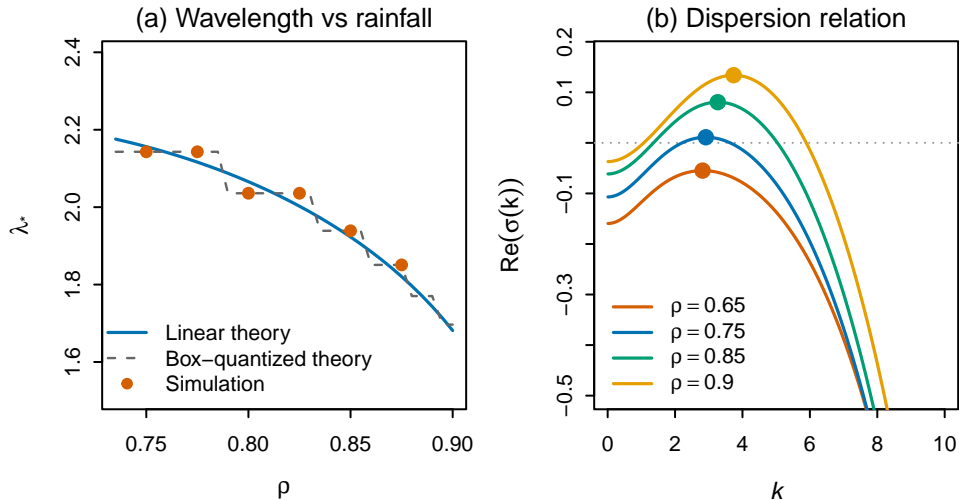


FIG. 3. Wavelength selection and rainfall dependence on a slope ($\Lambda_1 = 0.10$). (a) Dominant pattern wavelength λ_* versus dimensionless rainfall ρ : linear theory (blue curve), box-quantized admissible wavelengths L/n in the finite periodic domain (gray markers), and nonlinear PDE simulations (orange points). (b) Dispersion relation $\text{Re}[\sigma(k)]$ at four rainfall values. Filled circles mark the most unstable wavenumber $k_*(\rho)$. As aridity increases (decreasing ρ), the most unstable wavenumber k_* shifts to lower values, producing longer wavelengths at lower rainfall consistent with the Deblauwe trend. Note that the $\rho = 0.65$ curve peaks below zero (the uniform state is linearly stable at this rainfall), but the spectral peak still tracks the wavelength that would be selected by subcritical nucleation. Other parameters at baseline values (Table 4).

6.2. Band migration. The imaginary part of $\sigma(k)$ predicts uphill band migration driven by the advective water transport on the hillslope. The migration speed $c = -\text{Im}[\sigma(k_*)]/k_*$ depends on the hillslope advection parameter ν (dimensionless slope speed), and on flat terrain ($\nu = 0$) the migration should vanish.

Figure 4 shows spacetime plots of the vegetation field from two simulations: one on a slope ($\nu = 1$, $\Lambda_1 = 0.10$, $\chi = 2$) and one on flat terrain ($\nu = 0$, $\Lambda_1 = 0$, $\chi = 0$, $\Delta = 0$). The flat case sets $\Delta = 0$ to remove the vegetation-gradient deflection term, which would otherwise dominate directional transport when $\nu = 0$. It also sets $\chi = 0$ for conceptual consistency: χ enters only through the advection term $\nu(1 - \chi U)W$ and drops out when $\nu = 0$. Finally, $\rho = 0.5$ places the simulation within the flat-terrain instability window. The figure is therefore a qualitative demonstration of the slope–migration connection rather than a controlled single-parameter experiment. Diagonal stripes in the slope case show uphill migration; vertical stripes in the flat case confirm that migration vanishes without hillslope advection. We measure the migration speed from the simulation by tracking the phase of the dominant Fourier mode across time steps, obtaining $c \approx -0.004$. The speed is in the same direction as the linear prediction $c_{\text{lin}} = -\text{Im}[\sigma(k_*)]/k_* \approx -0.008$, with a factor-of-two discrepancy

in magnitude. Such discrepancies are typical when comparing linear-onset predictions with saturated nonlinear dynamics.

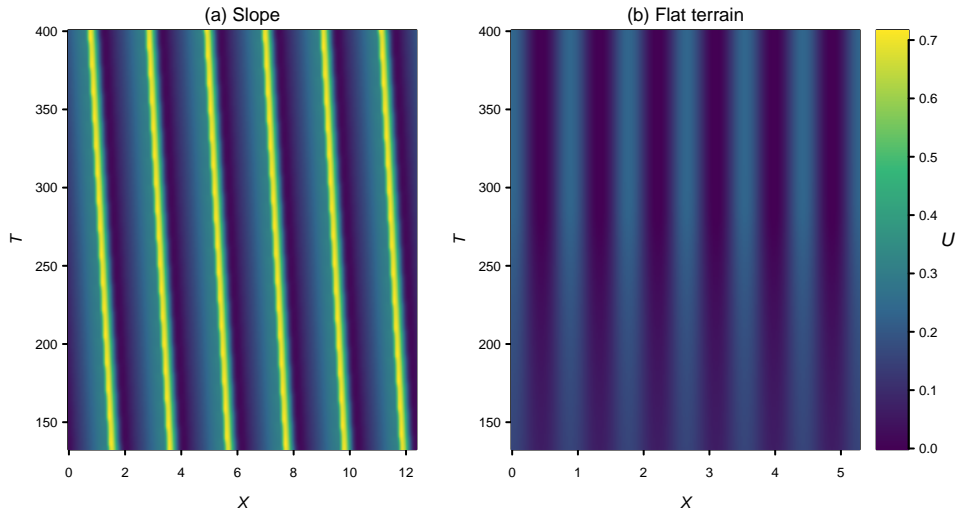


FIG. 4. Spacetime plots of $U(X, T)$ showing band migration. (a) Hillslope ($\nu = 1$, $\Lambda_1 = 0.10$, $\chi = 2$, $\rho = 0.8$): diagonal stripes indicate steady uphill migration. (b) Flat terrain ($\nu = 0$, $\Lambda_1 = 0$, $\chi = 0$, $\Delta = 0$, $\rho = 0.5$): stationary vertical bands. Other parameters at baseline values (Table 4).

6.3. Nonlinear branch structure. Linear stability analysis identifies the Turing-unstable boundary but says nothing about the amplitude or supercritical versus subcritical nature of the bifurcation. To explore the nonlinear branch structure, we follow a single-period stationary patterned equilibrium on flat terrain ($\Lambda_1 = 0$, $\nu = 0$), where patterns are stationary and the notion of a solution branch is well defined. We fix the computational domain to one wavelength at $\rho = 0.5$ (i.e., $L = \lambda_*(0.5)$), so that the branch being tracked is a one-period patterned state continued in ρ . This eliminates mode competition from multiple admissible integer stripe counts and yields a well-defined bifurcation diagram.

We perform two sweeps: forward continuation from the perturbed uniform state with increasing ρ , and backward continuation from an established finite-amplitude patterned state with decreasing ρ . Figure 5 shows the result. The one-period patterned branch exists over an interval $\rho \in [\rho_{\text{low}}, \rho_{\text{high}}]$, with a local amplitude peak near the lower end of the branch and a steep rise at higher rainfall. On an infinite domain, the linear onset of instability occurs at $\rho \approx 0.35$, but the single mode admitted by the one-period computational domain does not become linearly unstable until $\rho \approx 0.47$; the forward sweep therefore remains on the uniform branch until that point. The backward continuation sustains patterns down to $\rho \approx 0.42$, below this finite-domain onset, indicating a narrow hysteresis region consistent with subcritical bifurcation. Within this hysteresis interval the uniform state is unstable, so the patterned branch is the only attractor; the two arrows in Figure 5 mark the transitions between monostable and bistable regimes. The branch extends to approximately $\rho \approx 0.93$, near the upper edge of the linearly unstable interval.

Such behavior is consistent with other pattern-forming systems with fourth-order regularization [18]. These sweeps are exploratory time-marching computations, not rigorous arc-length continuation; spot checks at $N = 64$ produce the same qualitative

branch shape (G). The precise collapse-point locations and hysteresis width would require dedicated path-following methods, as in the rigorous existence and stability analysis of Sewalt and Doelman [20] for the Klausmeier–Gray–Scott system.

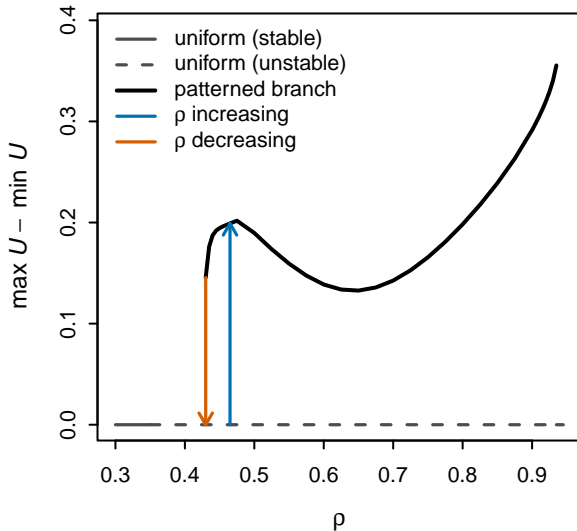


FIG. 5. *Nonlinear branch structure of a one-period stationary patterned equilibrium on flat terrain ($\Lambda_1 = 0$, $\nu = 0$): pattern amplitude ($\max U - \min U$) versus dimensionless rainfall ρ . The computational domain is one wavelength at $\rho = 0.5$. Gray line: spatially uniform vegetated state $U_0(\rho)$, shown solid where linearly stable and dashed where linearly unstable on an infinite domain; the finite-domain onset occurs at a higher ρ value, as discussed in the text. Black curve: patterned branch from backward continuation of a finite-amplitude state. The blue arrow marks the forward nucleation point (increasing ρ) and the orange arrow marks the apparent collapse point (decreasing ρ); the horizontal separation between the two arrows indicates a narrow hysteresis region consistent with subcritical bifurcation. The uniform branch represents the spatially homogeneous vegetation state $U_0(\rho)$; the bare-soil state $U = 0$, which also has zero amplitude, is not shown. Baseline parameters from Table 4 with $\Lambda_1 = 0$, $\nu = 0$; $N = 32$ grid points.*

7. Discussion. The framework operates at three layers of constraint: energy-balance sign constraints, gradient-expansion form for spatial terms, and a semilinear variational closure. The first two layers restrict the admissible model class independently of the closure; the semilinear family built from them shares a common water transfer function $\Phi(k)$ and a dispersion relation that decomposes into local and water-coupling contributions (section 4.2). The Euler–Lagrange representative is a specific choice from this family, and the concrete model analyzed here specializes further to plant-only energy balance ($s = 0$), frozen coupling amplitude η , and one spatial dimension. These results are properties of this representative, not universal consequences of the constrained class, but the layered progression makes explicit where physics ends and modeling begins—a distinction implicit when PDE terms are postulated directly.

What does the Euler–Lagrange closure buy, beyond selecting a specific model from the semilinear family? As shown in section 4.2, in the slope regime ($\Lambda_1 \neq 0$) the EL closure is essentially the unique choice of linearized derivative coefficients (m_0, n_0, r_0) that makes the local dispersion symbol even in wavenumber. This evenness forces the quartic coefficient to be nonpositive by construction. Beyond the structural advantages discussed in section 3, these algebraic constraints suggest an

in-principle empirical test. The coefficient relationships among A , D , E , B_0 , B_1 , B_2 are determined by the interaction lengths and the steady-state energy mismatch, so independent measurement of these quantities could test the EL closure against data.

The closure connects to an established methodology in mathematical physics. In condensed-matter theory, the Cahn–Hilliard [3], Allen–Cahn [1], and Swift–Hohenberg [22] models are constructed by writing a free energy from thermodynamic arguments and postulating gradient dynamics. For slow, overdamped systems, variational closure is a natural modeling choice. Vegetation dynamics, governed by growth and mortality on seasonal to decadal timescales, are slow, though slowness alone does not guarantee gradient-flow structure; ecological growth can be slow and still nonvariational. What makes the variational closure natural here is the combination of slowness with the energy-based structure derived in section 2. The mismatch penalties are physically motivated, the variational score functional is built from them, and gradient ascent is a natural low-order dynamics consistent with it. That said, the EL closure is an algebraically motivated ansatz, not a derivation from variational principles of the coupled system: the score functional operates on vegetation at fixed water, and we impose the quasi-steady water coupling separately. The useful properties it delivers—even local symbol, nonpositive quartic, exact decomposition—are algebraic consequences of this ansatz, testable against data independently of its variational motivation.

The Klausmeier model and its variants have been enormously successful at capturing vegetation pattern phenomenology with minimal postulated structure. Our framework asks a complementary question: which parts of that phenomenological structure can be recovered or constrained from upstream physical principles, and what additional structure emerges when the constraints are imposed? Some familiar terms reappear, in particular the water-mediated positive feedback and the short-wavelength cutoff that together produce the finite-wavenumber instability. But the energy balance framework also constrains the relationships among coefficients and yields a mechanism decomposition with regime-dependent structure. The reduction to a small number of length-scale and coupling parameters, some with signs constrained by energy-balance reasoning and others with interpretable regime-dependent signs, provides an organizing principle for a field in which many distinct models reproduce similar phenomenology.

The mechanism decomposition (4.12) and its regime dependence—energy-balance coupling dominant when $\Lambda_1 = 0$, water-mediated coupling dominant when $\Lambda_1 > 0$ —persist across the parameter regimes we have examined. In the slope regime, the model recovers the empirically correct rainfall–wavelength trend [8]. Whether this regime dependence has quantitative ecological consequences depends on the specific ecosystem and on the values of the interaction parameters, which have not yet been estimated from field data.

The framework generates several testable predictions. In the slope regime where the water-mediated coupling dominates wavelength selection, the model yields $d\lambda_*/d\rho < 0$: longer wavelength at lower rainfall, consistent with remote sensing data [8]. This is a parameter-regime prediction, not a universal property of the model; it requires Λ_1 large enough to reduce the local even contribution D , which is the physically relevant regime for sloped terrain. The imaginary part of $\sigma(k)$ predicts uphill band migration on slopes and no migration on flat terrain, consistent with field observations [8, 23]. A potentially distinguishing test concerns wavelength scaling: in the Klausmeier model, the wavelength scales with a postulated plant diffusion coefficient, while in our model it depends on the interaction lengths ℓ_1 and ℓ_2 . Independent estimation of the plant–plant interaction range from canopy radius data or

microclimate transects could distinguish the two frameworks. The water deflection term $J_2 u_x = -\delta_0 w u_x$ predicts that overland flow responds to vegetation *gradients*, not just to local density; measuring this relationship in the field would provide a direct test.

Several directions remain open. Rigorous existence, uniqueness, and stability analysis of patterned solutions [20] would put the nonlinear branch structure on firm ground. The framework extends naturally to two spatial dimensions, but we leave that analysis to future work. Incorporating the soil energy penalty ($s > 0$) would test whether the soil–plant coupling modifies the instability mechanisms or introduces new ones. Calibrating the model requires estimating the gradient-expansion coefficients from ecophysiological data; until then, the predictions remain qualitative.

Finally, the variational origin and fourth-order regularization suggest structural connections to the Cahn–Hilliard [3] and Swift–Hohenberg [22] families of pattern-forming PDEs. The coupled dynamics are not a single-field gradient flow, since the quasi-steady water coupling breaks self-adjointness and this breaking is essential for band migration. Nevertheless, the shared features of fourth-order regularization and wavelength selection from a variational score functional suggest that tools from variational pattern-forming theory may apply. Whether \mathcal{E} can serve as a Lyapunov functional for the coupled system remains open.

8. Conclusion. Energy balance, water conservation, and gradient expansion sharply constrain the admissible class of dryland vegetation models before any closure is chosen. The Euler–Lagrange representative of this constrained class yields an exactly decomposable dispersion relation with three instability mechanisms, one of which—energy-balance spatial coupling—is regime-dependent and absent from standard phenomenological models. On slopes, the model recovers the empirically correct rainfall–wavelength trend and uphill band migration; nonlinear simulations confirm the linear predictions, and exploratory continuation reveals a narrow hysteresis region consistent with subcritical bifurcation.

These results do not derive a unique first-principles vegetation equation. They show, instead, that upstream physical constraints can organize the space of plausible models, separating structure that is physically enforced from structure that requires a modeling choice. The framework suggests a path toward ecological pattern models that are more structured than purely phenomenological formulations while remaining analyzable with the tools of variational pattern-forming PDE theory.

Acknowledgments. The author used Claude (Anthropic, Claude Opus 4) for manuscript editing assistance, including sentence-level revisions, style auditing, and checking for internal mathematical consistency. All output was verified by the author, who takes full responsibility for the content.

References.

- [1] Allen, S. M. and Cahn, J. W. (1979). A microscopic theory for antiphase boundary motion and its application to antiphase domain coarsening. *Acta Metallurgica*, 27(6):1085–1095.
- [2] Borgogno, F., D’Odorico, P., Laio, F., and Ridolfi, L. (2009). Mathematical models of vegetation pattern formation in ecohydrology. *Reviews of Geophysics*, 47(1):RG1005.
- [3] Cahn, J. W. and Hilliard, J. E. (1958). Free energy of a nonuniform system. I. Interfacial free energy. *The Journal of Chemical Physics*, 28(2):258–267.

- [4] Campbell, G. S. and Norman, J. M. (1998). *An Introduction to Environmental Biophysics*. Springer, New York, 2nd edition.
- [5] Canuto, C., Hussaini, M. Y., Quarteroni, A., and Zang, T. A. (2006). *Spectral Methods: Fundamentals in Single Domains*. Springer, Berlin.
- [6] Cox, S. M. and Matthews, P. C. (2002). Exponential time differencing for stiff systems. *Journal of Computational Physics*, 176(2):430–455.
- [7] Deblauwe, V., Barbier, N., Couteron, P., Lejeune, O., and Bogaert, J. (2008). The global biogeography of semi-arid periodic vegetation patterns. *Global Ecology and Biogeography*, 17(6):715–723.
- [8] Deblauwe, V., Couteron, P., Bogaert, J., and Barbier, N. (2012). Determinants and dynamics of banded vegetation pattern migration in arid climates. *Ecological Monographs*, 82(1):3–21.
- [9] Gandhi, P., Iams, S., Bonetti, S., and Silber, M. (2019). Vegetation pattern formation in drylands. In D’Odorico, P., Porporato, A., and Wilkinson Runyan, C., editors, *Dryland Ecohydrology*, pages 469–509. Springer, Cham.
- [10] Gandhi, P., Oline, M., and Silber, M. (2025). A flow-kick model of dryland vegetation patterns: the impact of rainfall variability on resilience. *SIAM Journal on Applied Dynamical Systems*, 24(4):3092–3126.
- [11] Gilad, E., von Hardenberg, J., Provenzale, A., Shachak, M., and Meron, E. (2004). Ecosystem engineers: from pattern formation to habitat creation. *Physical Review Letters*, 93(9):098105.
- [12] Gilad, E., von Hardenberg, J., Provenzale, A., Shachak, M., and Meron, E. (2007). A mathematical model for plants as ecosystem engineers. *Journal of Theoretical Biology*, 244(4):680–691.
- [13] Gowda, K., Chen, Y., Iams, S., and Silber, M. (2016). Assessing the robustness of spatial pattern sequences in a dryland vegetation model. *Proceedings of the Royal Society A*, 472(2187):20150893.
- [14] Jones, H. G. (2013). *Plants and Microclimate: A Quantitative Approach to Environmental Plant Physiology*. Cambridge University Press, 3rd edition.
- [15] Kassam, A.-K. and Trefethen, L. N. (2005). Fourth-order time-stepping for stiff PDEs. *SIAM Journal on Scientific Computing*, 26(4):1214–1233.
- [16] Klausmeier, C. A. (1999). Regular and irregular patterns in semiarid vegetation. *Science*, 284(5421):1826–1828.
- [17] Meron, E. (2012). *Nonlinear Physics of Ecosystems*. CRC Press.
- [18] Meron, E. (2018). From patterns to function in living systems: Dryland ecosystems as a case study. *Annual Review of Condensed Matter Physics*, 9:79–103.
- [19] Rietkerk, M., Boerlijst, M. C., van Langevelde, F., HilleRisLambers, R., van de Koppel, J., Kumar, L., Prins, H. H. T., and de Roos, A. M. (2002). Self-organization of vegetation in arid ecosystems. *The American Naturalist*, 160(4):524–530.
- [20] Sewalt, L. and Doelman, A. (2017). Spatially periodic multipulse patterns in a generalized Klausmeier–Gray–Scott model. *SIAM Journal on Applied Dynamical Systems*, 16(2):1113–1163.
- [21] Sherratt, J. A. (2005). An analysis of vegetation stripe formation in semi-arid landscapes. *Journal of Mathematical Biology*, 51(2):183–197.
- [22] Swift, J. and Hohenberg, P. C. (1977). Hydrodynamic fluctuations at the convective instability. *Physical Review A*, 15(1):319–328.
- [23] Valentin, C., d’Herbès, J.-M., and Poesen, J. (1999). Soil and water components of banded vegetation patterns. *Catena*, 37(1–2):1–24.
- [24] von Hardenberg, J., Meron, E., Shachak, M., and Zarmi, Y. (2001). Diversity of

vegetation patterns and desertification. *Physical Review Letters*, 87(19):198101.

Appendix A. Linearization of the water equation.

To obtain the water transfer function $\Phi(k)$, we substitute $U = U_0 + \epsilon \hat{U} e^{ikX}$ and $W = W_0 + \epsilon \hat{W} e^{ikX}$ into the quasi-steady water equation (3.10) and collect terms at $O(\epsilon)$. The advection flux $\nu(1 - \chi U)W$ linearizes to produce contributions from two sources: a \hat{W} term from water perturbations at fixed vegetation, and a \hat{U} term from vegetation perturbations at fixed water. Writing $c_0 = \nu - \chi\nu U_0$ for the effective advection speed at the steady state, the linearized water equation becomes

$$(A.1) \quad (ic_0k + \mathcal{D}k^2)\hat{W} + (\Delta W_0k^2 - i\chi\nu W_0k)\hat{U} = -(1 + \beta U_0)\hat{W} - \beta W_0\hat{U}.$$

Solving for \hat{W} gives the water transfer function

$$(A.2) \quad \Phi(k) = \frac{\hat{W}}{\hat{U}} = \frac{-W_0(\beta + \Delta k^2 - i\chi\nu k)}{1 + \beta U_0 + \mathcal{D}k^2 + ic_0k}.$$

Compared to the classical case without vegetation obstruction ($\chi = 0$), the vegetation obstruction adds $-i\chi\nu k$ to the numerator and replaces ν by $c_0 = \nu(1 - \chi U_0)$ in the denominator. The numerator correction modifies the real part of the water coupling at finite k , providing a rainfall-dependent contribution to wavelength selection that is absent when $\chi = 0$. When $\mathcal{D} = \Delta = \chi = 0$, this reduces to $\Phi(k) = -\beta W_0/(1 + \beta U_0 + i\nu k)$.

Appendix B. Linearization of the Euler–Lagrange operator.

To obtain the linearized growth rate $\sigma(k)$, we linearize the Euler–Lagrange operator

$$(B.1) \quad F(U, W) = \frac{\partial \mathcal{L}}{\partial U} - \frac{d}{dX} \frac{\partial \mathcal{L}}{\partial U_X} + \frac{d^2}{dX^2} \frac{\partial \mathcal{L}}{\partial U_{XX}}$$

with W treated as an independent external field, and then substitute $\delta W = \Phi(k) \delta U$. Although G contains the asymmetric term $\eta \Lambda_1 U_X$, the alternating-sign structure of the Euler–Lagrange operator (B.1) forces all odd-in- k contributions from the local part to cancel. This is verified explicitly in section C. Consequently, the Fourier symbol of the local (water-independent) linearized operator is real and even in k , contributing only even powers k^0, k^2, k^4 .

All imaginary (odd-in- k) contributions to $\sigma(k)$ come from water coupling $\mathcal{B}(k)\Phi(k)$ through three channels. The advective ik term in $\Phi(k)$'s denominator and the $-i\chi\nu k$ term in $\Phi(k)$'s numerator both make Φ complex when $\nu \neq 0$. The $B_1(ik)$ factor in $\mathcal{B}(k)$ contributes an imaginary part when $\Lambda_1 \neq 0$, even if Φ were real. All three channels require the water coupling; none arises from the local part of the linearized operator. In particular, band migration is driven by the water response on the hill-slope, not by the asymmetric interaction length Λ_1 acting through the local energy functional. Instead, Λ_1 enters through the *even* coefficient $D = 2\eta\Lambda_2q - \eta^2\Lambda_1^2$. It modifies the balance between destabilizing and stabilizing contributions to the local part of $\sigma(k)$, not the propagation speed.

Appendix C. Cancellations in the linearized Euler–Lagrange operator.

This section verifies two structural properties of the linearized Euler–Lagrange operator. First, all odd-in- k contributions from the local part cancel. Second, terms involving $\eta'(U_0)$ reduce to an even k^2 residual whose consequences are analyzed in section C.6.

C.1. Setup. With $\mathcal{L} = \mu U - \frac{1}{2}G^2$ and $G = g(U, W) + \eta(U, W)(\Lambda_1 U_X + \Lambda_2 U_{XX})$, the Euler–Lagrange operator is

$$(C.1) \quad F = \frac{\partial \mathcal{L}}{\partial U} - \frac{d}{dX} \frac{\partial \mathcal{L}}{\partial U_X} + \frac{d^2}{dX^2} \frac{\partial \mathcal{L}}{\partial U_{XX}}.$$

At the uniform state, $U_{0X} = U_{0XX} = 0$, so $G_0 = g(U_0, W_0)$. We treat W as an independent external field and linearize in δU , δW separately. Throughout this section we write $\eta_0 = \eta(U_0, W_0)$ for the steady-state value of the spatial coupling amplitude; the main text denotes this quantity simply by η after freezing.

C.2. The three Euler–Lagrange contributions. We need the partial derivatives of \mathcal{L} :

$$(C.2) \quad \frac{\partial \mathcal{L}}{\partial U} = \mu - G[g_U + \eta_U(\Lambda_1 U_X + \Lambda_2 U_{XX})],$$

$$(C.3) \quad \frac{\partial \mathcal{L}}{\partial U_X} = -G \eta(U, W) \Lambda_1,$$

$$(C.4) \quad \frac{\partial \mathcal{L}}{\partial U_{XX}} = -G \eta(U, W) \Lambda_2,$$

where $\eta_U = \partial \eta / \partial U$ at fixed W . The $\partial \eta / \partial W$ derivative does not enter because W is treated as an external field in the semilinear Euler–Lagrange operator. Linearizing each around the uniform state ($G = G_0$, $\eta = \eta_0$, $\eta_U = \eta_{0,U}$, $g_U = q$) and substituting $\delta U \rightarrow e^{ikX}$, $\delta U_X \rightarrow (ik)e^{ikX}$, $\delta U_{XX} \rightarrow -k^2 e^{ikX}$:

C.3. Contribution from $\partial \mathcal{L} / \partial U$. Linearizing and keeping only terms that depend on $\eta_{0,U}$:

$$(C.5) \quad \delta \left(\frac{\partial \mathcal{L}}{\partial U} \right) \Big|_{\eta_U} = -G_0 \eta_{0,U} [\Lambda_1(ik) - \Lambda_2 k^2] \delta U.$$

C.4. Contribution from $-\partial_X(\partial \mathcal{L} / \partial U_X)$. Differentiating (C.3), the η_U variation at the uniform state gives:

$$(C.6) \quad -\frac{d}{dX} \left(\frac{\partial \mathcal{L}}{\partial U_X} \right) \Big|_{\eta_U} = +(ik) G_0 \eta_{0,U} \Lambda_1 \delta U.$$

C.5. Contribution from $+\partial_X^2(\partial \mathcal{L} / \partial U_{XX})$. From (C.4), $\partial \mathcal{L} / \partial U_{XX} = -G \eta \Lambda_2$. The η_U variation at the uniform state is $-G_0 \eta_{0,U} \Lambda_2 \delta U$. Applying $+d^2/dX^2$ (i.e., multiplying by $(ik)^2 = -k^2$):

$$(C.7) \quad \frac{d^2}{dX^2} \left(\frac{\partial \mathcal{L}}{\partial U_{XX}} \right) \Big|_{\eta_U} = -k^2 (-G_0 \eta_{0,U} \Lambda_2 \delta U) = +k^2 G_0 \eta_{0,U} \Lambda_2 \delta U.$$

C.6. Residual $\eta_{0,U}$ terms. Summing the three $\eta_{0,U}$ contributions:

$$(C.8) \quad \begin{aligned} & -G_0 \eta_{0,U} [\Lambda_1(ik) - \Lambda_2 k^2] + G_0 \eta_{0,U} \Lambda_1(ik) + G_0 \eta_{0,U} \Lambda_2 k^2 \\ & = G_0 \eta_{0,U} [-\Lambda_1(ik) + \Lambda_2 k^2 + \Lambda_1(ik) + \Lambda_2 k^2] = 2G_0 \eta_{0,U} \Lambda_2 k^2. \end{aligned}$$

The odd-in- k terms ($\Lambda_1(ik)$) cancel exactly, but the even k^2 contributions add rather than cancel. Since the semilinear Euler–Lagrange operator treats W as an external field, $\partial \eta / \partial W$ does not enter the operator, and the W -dependence of η is irrelevant.

The residual (C.8) is a real, even k^2 correction. If η were kept state-dependent, it would shift the quadratic coefficient to

$$(C.9) \quad D_{\text{full}} = D_{\text{frozen}} + 2G_0\eta_0 U \Lambda_2,$$

where $D_{\text{frozen}} = 2\eta_0\Lambda_2q - \eta_0^2\Lambda_1^2$ is the coefficient reported in the main text. The frozen- η closure sets this correction to zero. On the lower vegetated branch, $G_0 = \mu/q$, and in the weak-penalty regime $\mu \ll 1$ the correction is $O(\mu)$ relative to the retained terms in D , provided η varies on an $O(1)$ state scale. The residual does not affect the even parity of $\mathcal{A}(k)$, the nonpositive quartic coefficient $E = -\eta_0^2\Lambda_2^2$, or the fact that all odd-in- k contributions arise through the water coupling.

C.7. Cancellation of odd-in- k local terms. With $\eta = \eta_0$ constant, the linearized operator (treating W as external) is

$$(C.10) \quad \delta F = [-q + \eta_0\Lambda_1(ik) + \eta_0\Lambda_2k^2] \delta G - G_0 \delta g_U,$$

where $\delta G = [q + \eta_0\Lambda_1(ik) - \eta_0\Lambda_2k^2] \delta U + g_W \delta W$ and $\delta g_U = g_{UU} \delta U + g_{UW} \delta W$. The minus sign on $G_0 \delta g_U$ arises because $\delta(\partial\mathcal{L}/\partial U) = -g_U \delta G - G_0 \delta g_U$. The local part (setting $\delta W = 0$) is the product

$$(C.11) \quad [-q + \eta_0\Lambda_1(ik) + \eta_0\Lambda_2k^2] \cdot [q + \eta_0\Lambda_1(ik) - \eta_0\Lambda_2k^2] - G_0 g_{UU}.$$

Expanding the product, the $(ik)^1$ cross-terms are

$$(C.12) \quad (-q) \cdot \eta_0\Lambda_1(ik) + \eta_0\Lambda_1(ik) \cdot q = 0,$$

and the $(ik)^3$ cross-terms are

$$(C.13) \quad \eta_0\Lambda_1(ik) \cdot (-\eta_0\Lambda_2k^2) + \eta_0\Lambda_2k^2 \cdot \eta_0\Lambda_1(ik) = 0.$$

All odd powers of k cancel, leaving only even powers. The surviving terms give

$$(C.14) \quad A + Dk^2 + Ek^4 = (-q^2 + G_0) + (2\eta_0\Lambda_2q - \eta_0^2\Lambda_1^2)k^2 - \eta_0^2\Lambda_2^2k^4,$$

confirming the coefficients stated in the main text.

Appendix D. Derivation of the water-coupling coefficients.

The dispersion relation (4.12) involves the water-coupling polynomial $\mathcal{B}(k) = B_0 + B_1(ik) + B_2k^2$. This section derives B_0 , B_1 , B_2 from the linearized Euler-Lagrange operator.

With η frozen (justified by section C), the linearized operator evaluated at the uniform state is

$$(D.1) \quad \delta F = [-q + \eta\Lambda_1(ik) + \eta\Lambda_2k^2] \delta G - G_0 \delta g_U,$$

where $\delta G = [q + \eta\Lambda_1(ik) - \eta\Lambda_2k^2] \delta U + g_W \delta W$ and $\delta g_U = g_{UU} \delta U + g_{UW} \delta W$. The water-coupling coefficient $\mathcal{B}(k)$ collects the terms proportional to δW :

$$(D.2) \quad \mathcal{B}(k) = [-q + \eta\Lambda_1(ik) + \eta\Lambda_2k^2] g_W - G_0 g_{UW}.$$

From the nondimensional mismatch $G = -\Gamma + U - \frac{1}{2}U^2 - UW + \eta(\Lambda_1U_X + \Lambda_2U_{XX})$, the local part $g(U, W) = -\Gamma + U - \frac{1}{2}U^2 - UW$ gives $g_W = -U_0$ and $g_{UW} = -1$ at the steady state. Substituting:

$$(D.3) \quad \begin{aligned} \mathcal{B}(k) &= [-q + \eta\Lambda_1(ik) + \eta\Lambda_2k^2] (-U_0) - G_0 (-1) \\ &= (qU_0 + G_0) + (-\eta\Lambda_1 U_0)(ik) + (-\eta\Lambda_2 U_0) k^2, \end{aligned}$$

yielding

$$(D.4) \quad B_0 = qU_0 + G_0, \quad B_1 = -\eta\Lambda_1 U_0, \quad B_2 = -\eta\Lambda_2 U_0.$$

The coefficient B_0 combines the direct water–vegetation coupling (qU_0 , from g_W acting through the EL variation of G) with the mismatch correction (G_0 , from the linearization of g_U with respect to W). The spatial coefficients B_1 and B_2 arise because the EL operator’s derivative terms $-\partial_X(\partial\mathcal{L}/\partial U_X)$ and $+\partial_X^2(\partial\mathcal{L}/\partial U_{XX})$ act on the water-dependent part of G , making the coupling strength k -dependent. When $\Lambda_1 = 0$ (flat terrain), $B_1 = 0$ and the water coupling is even in k .

Appendix E. Structural comparison with the Klausmeier model.

Table 5 presents a term-by-term comparison of the Klausmeier model with the energy-balance model in the quasi-steady regime ($s = 0$). The $\beta_1 w w$ term plays the same structural role as the Klausmeier uptake $\beta_K u^2 w$; the different power of u reflects different density-dependence assumptions, but both are consistent with the sign constraints.

TABLE 5
Structural comparison of the Klausmeier model and the energy balance model.

Feature	Klausmeier	Energy balance
Growth	$\beta_K u^2 w$ (postulated)	From G_2 ; sign-constrained
Mortality	$-m u$ (postulated)	From energy mismatch penalty
Water uptake	$-\beta_K u^2 w$ (postulated)	From quasi-steady conservation
Rainfall	a (parameter)	R (parameter)
Water loss	$-\mu_K w$ (postulated)	$-\mu(u)w$ (from general L)
Water transport	$v w_x + D_w w_{xx}$ (postulated)	From gradient expansion of J
Deflection	Absent	$-\delta_0 w u_x$ (gradient expansion)
Spatial terms	$D_u u_{xx}$ (postulated dispersal)	From gradient expansion of energy fluxes
Highest order	k^2 (second; postulated)	k^4 (fourth; variational)
Instability mechanisms	1 (water-mediated)	3 (exact decomposition (4.12))
Constraints	All terms postulated	Some signs fixed by energy balance

These differences are visible when the dispersion curves are normalized by k_* and σ_{\max} (Figure 6). Both models are evaluated on the upper vegetated branch, which is the ecologically relevant pattern-forming branch in each case [21]. Both have $\sigma(0) < 0$, confirming that the instability is of Turing (differential-flow) type rather than a spatially uniform saddle-point instability. The energy balance model has a narrow instability band centered at $k/k_* = 1$, while the Klausmeier instability band is a broader dome extending to approximately $k/k_* \approx 3$. The difference in bandwidth reflects the stabilization mechanism: a single k^2 plant-diffusion term in the Klausmeier model provides a relatively gentle high- k cutoff, whereas the fourth-order variational term in the energy balance model produces a sharper cutoff and tighter wavenumber selection. A narrow instability band constrains the selected wavelength tightly, while a broad band permits greater variability in the realized pattern.

Appendix F. Admissible parameter regime.

The linear stability analysis identifies when patterns form, but not whether the resulting nonlinear PDE remains well-posed during finite-amplitude evolution. We

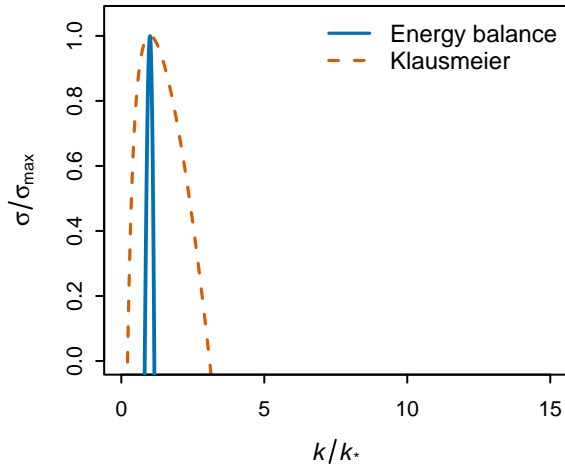


FIG. 6. Normalized dispersion relations: σ/σ_{\max} versus k/k_* for the energy balance model (blue solid; $\Lambda_1 = 0$, $\Lambda_2 = 0.01$, other parameters at baseline from Table 5 of the main text including $\nu = 1$) and the Klausmeier model (orange dashed; $a = 1.5$, $m = 0.45$, $v = 182.5$, $D_u = 1$). Both models are evaluated on the upper vegetated branch; the Klausmeier parameters are representative values from the literature [21]. The energy balance instability band is a sharp spike at $k/k_* = 1$; the Klausmeier band is a broad dome. The normalization by σ_{\max} shows only the positive part of each curve.

develop heuristic admissibility constraints by examining when the quasi-steady water operator retains its coercivity structure. The semilinear closure (3.3) requires solving the quasi-steady water equation at each time step, and the coercivity of that equation depends on the vegetation field $U(X)$ through the spatially varying operator coefficients.

Writing the water equation in the form

$$(F.1) \quad -\mathcal{D} W_{XX} + a(X) W_X + b(X) W = \rho,$$

where $a(X) = \nu(1 - \chi U) - \Delta U_X$ and $b(X) = 1 + \beta U - \nu \chi U_X - \Delta U_{XX}$. The operator is expected to remain well-conditioned when $b(X) > 0$ everywhere. This is a sufficient condition for coercivity in the constant-coefficient case and a reasonable diagnostic for the variable-coefficient setting used here. At the uniform steady state, $b = 1 + \beta U_0 > 0$; the question is whether $b(X)$ can become negative as the pattern develops.

For a saturated vegetation pattern $U \approx U_0 + \mathcal{A} \cos(k_* X)$ with amplitude \mathcal{A} , the coefficient $b(X)$ becomes

$$(F.2) \quad b(X) \approx 1 + \beta U_0 + \mathcal{A}[(\beta + \Delta k_*^2) \cos(k_* X) + \nu \chi k_* \sin(k_* X)].$$

The minimum of this harmonic expression is

$$(F.3) \quad b_{\min} \approx 1 + \beta U_0 - \mathcal{A} \sqrt{(\beta + \Delta k_*^2)^2 + (\nu \chi k_*)^2}.$$

All three terms under the radical contribute: the β and Δk_*^2 terms shift the minimum away from the inflection points of U , while the $\nu \chi k_*$ term captures the vegetation-obstruction gradient. When the obstruction term dominates ($\nu \chi k_* \gg \beta + \Delta k_*^2$), the minimum occurs near the inflection points of U and (F.3) reduces to $b_{\min} \approx 1 + \beta U_0 - \nu \chi k_* \mathcal{A}$.

The condition $b_{\min} > 0$ gives the admissibility constraint

$$(F.4) \quad \mathcal{A} \sqrt{(\beta + \Delta k_*^2)^2 + (\nu \chi k_*)^2} < 1 + \beta U_0.$$

The wavenumber k_* depends on the rainfall parameter ρ through the dispersion relation, while the saturated amplitude \mathcal{A} depends on the distance from the instability threshold. This constraint couples the obstruction strength χ to the selected spatial structure of the pattern. In the slope regime where k_* increases with ρ (see the main text), the constraint becomes tighter at higher rainfall.

A second, independent constraint ensures that the effective advection coefficient $a(X)$ does not reverse sign. Under the same cosine ansatz,

$$(F.5) \quad a(X) \approx \nu(1 - \chi U_0) + \mathcal{A}[-\nu \chi \cos(k_* X) + \Delta k_* \sin(k_* X)],$$

so the harmonic minimum is

$$(F.6) \quad a_{\min} \approx \nu(1 - \chi U_0) - \mathcal{A} \sqrt{(\nu \chi)^2 + (\Delta k_*)^2}.$$

The condition $a_{\min} > 0$ gives the advection admissibility constraint

$$(F.7) \quad \mathcal{A} \sqrt{(\nu \chi)^2 + (\Delta k_*)^2} < \nu(1 - \chi U_0).$$

When Δk_* is small compared to $\nu \chi$, the minimum occurs near the vegetation peaks and (F.7) reduces to $\chi(U_0 + \mathcal{A}) < 1$. Advection reversal does not make the operator singular (diffusion $\mathcal{D}W_{XX}$ provides elliptic regularization) but increases condition number, signaling that the expansion $J_0(u, w) = v_0 w - v_1 u w$ is beyond its valid domain. Physically, $\chi U > 1$ would mean that vegetation obstructs more overland flow than exists—an extrapolation artifact of the linear truncation in (2.11).

The constraints (F.4)–(F.7) restrict the admissible combinations of χ , k_* , and the pattern amplitude, and they tighten as k_* increases. In the numerical simulations, we verify that $\chi = 2$ satisfies both constraints at all computed parameter values.

Appendix G. Numerical method details.

G.1. Water operator and linear system. The periodic domain is discretized with N uniformly spaced points. Given the current vegetation field U , the water conservation equation (3.10) is linear in W and can be written as a dense $N \times N$ linear system

$$(G.1) \quad \mathbf{A}(U) \mathbf{W} = \rho \mathbf{1},$$

where D_1 and D_2 are spectral first- and second-derivative matrices constructed from the Fourier wavenumbers, and the operator $\mathbf{A}(U)$ is

$$(G.2) \quad \mathbf{A}(U) = -\mathcal{D} D_2 + \text{diag}(\nu(1 - \chi U) - \Delta U_X) D_1 + \text{diag}(1 + \beta U - \nu \chi U_X - \Delta U_{XX}).$$

This system is solved by direct factorization at each time step (cost $O(N^3)$, negligible for $N \leq 512$).

G.2. Frozen-linearization semilinear split. Time integration uses a semi-linear decomposition of the vegetation equation dynamics. The right-hand side is decomposed into a linear part L_k and a nonlinear remainder N_k in Fourier space. The linear operator is the dispersion relation *frozen at the uniform steady state*,

$$(G.3) \quad L_k = \sigma(k),$$

where $\sigma(k)$ is given by the dispersion relation in the main text. This is a linearization about (U_0, W_0) , not an exact decomposition of the state-dependent nonlinear operator. Away from the uniform state, the “nonlinear remainder” $N_k = \widehat{F}(U) - L_k \hat{v}_k$ contains contributions that are formally linear in the perturbation $\hat{v}_k = \widehat{U - U_0}$. This frozen-linearization approach is standard for exponential time differencing methods applied to pattern-forming PDEs. Its advantage is that the stiff fourth-order term $E k^4$ and the water coupling $\mathcal{B}(k)\Phi(k)$ are handled by the matrix exponential, while the nonlinear remainder is smooth and amenable to explicit Runge–Kutta stages.

G.3. ETDRK4 stage structure. The ETDRK4 update at each time step involves four evaluations of N_k , each requiring one quasi-steady water solve and one evaluation of the nonlinear right-hand side. These evaluations are combined with the exponential propagators $e^{L_k h}$ and $e^{L_k h/2}$ and three auxiliary coefficient functions. All exponential-related coefficients are computed via the Kassam–Trefethen contour integral with $M = 32$ quadrature points to avoid cancellation errors near $L_k \approx 0$.

G.4. Periodic domain and η freezing. The periodic setting represents a local patch of a long hillslope far from the boundaries. The explicit hillslope solution derived in the main text is illustrative and is not used in the numerics. The spatial correction amplitude η is frozen at its steady-state value in both the linear operator and the nonlinear right-hand side. As shown in section C, state-dependent η would contribute an even k^2 correction to the quadratic coefficient D ; freezing η removes this correction while preserving the parity structure and the nonpositive quartic. In the weak-penalty regime ($\mu \ll 1$), the correction is asymptotically small on the lower vegetated branch. Beyond linear order, freezing η is a further simplification relative to the state-dependent $\eta(U, W)$ in the original functional.

G.5. Additional numerical parameters. Initial conditions are $U(X, 0) = U_0 + 0.01 \xi(X) + 0.02 \cos(k_* X)$, where ξ is white noise and k_* is rounded to the nearest box-quantized wavenumber $2\pi n/L$ to ensure periodicity on the computational domain. The dominant wavelength is extracted from the peak of the spatial power spectrum of the final state, and the migration speed by tracking the phase of the dominant Fourier mode across time steps. Integration terminates early when the relative change in pattern amplitude $\max U - \min U$ falls below 5×10^{-3} over three consecutive checks spaced $T = 100$ apart. For the bifurcation sweeps, the rainfall parameter ρ is incremented in steps of 0.025, with finer steps of 0.005 near the fold region. The bifurcation computation uses $N = 32$ on a one-period domain; spot checks at $N = 64$ produce the same qualitative hysteresis picture. We checked that the reported wavelength and migration speed change by less than 2% when halving h or doubling N at selected parameter values.